

AD \_\_\_\_\_

GRANT NUMBER DAMD17-94-J-4424

TITLE: Single-Pulse Dual-Energy Mammography Using a Binary Screen Coupled to Dual CCD Cameras

PRINCIPAL INVESTIGATOR: John M. Boone, Ph.D.

CONTRACTING ORGANIZATION: University of California  
Davis, California 95616

REPORT DATE: August 1998

TYPE OF REPORT: Annual

PREPARED FOR: Commander  
U.S. Army Medical Research and Materiel Command  
Fort Detrick, Frederick, Maryland 21702-5012

DISTRIBUTION STATEMENT: Approved for public release;  
distribution unlimited

The views, opinions and/or findings contained in this report are those of the author(s) and should not be construed as an official Department of the Army position, policy or decision unless so designated by other documentation.

# REPORT DOCUMENTATION PAGE

*Form Approved*  
OMB No. 0704-0188

Public reporting burden for this collection of information is estimated to average 1 hour per response, including the time for reviewing instructions, searching existing data sources, gathering and maintaining the data needed, and completing and reviewing the collection of information. Send comments regarding this burden estimate or any other aspect of this collection of information, including suggestions for reducing this burden, to Washington Headquarters Services, Directorate for Information Operations and Reports, 1215 Jefferson Davis Highway, Suite 1204, Arlington, VA 22202-4302, and to the Office of Management and Budget, Paperwork Reduction Project (0704-0188), Washington, DC 20503.

1. AGENCY USE ONLY <i>(Leave blank)</i>			2. REPORT DATE August 1998		3. REPORT TYPE AND DATES COVERED Annual (15 Jul 97 - 14 Jul 98)	
4. TITLE AND SUBTITLE  Single-Pulse Dual-Energy Mammography Using a Binary Screen Coupled to Dual CCD Cameras			5. FUNDING NUMBERS  DAMD17-94-J-4424			
6. AUTHOR(S)  John M. Boone, Ph.D.			8. PERFORMING ORGANIZATION REPORT NUMBER			
7. PERFORMING ORGANIZATION NAME(S) AND ADDRESS(ES)  University of California Davis, California 95616			10. SPONSORING/MONITORING AGENCY REPORT NUMBER			
9. SPONSORING/MONITORING AGENCY NAME(S) AND ADDRESS(ES)  Commander U. S. Army Medical Research and Materiel Command Fort Detrick, Frederick, Maryland 21702-5012			12a. DISTRIBUTION / AVAILABILITY STATEMENT  Approved for public release; distribution unlimited			
11. SUPPLEMENTARY NOTES						
12b. DISTRIBUTION CODE				13. ABSTRACT <i>(Maximum 200)</i>  <p>This is the fourth annual report for this four-year grant, however a one-year no cost extension was requested and approved. The original goals of this grant (circa 1993) were based upon the use of dual CCD cameras for the digital mammographic acquisition. After studying the CCD detector, and in consideration of recent developments in detector technology, we have abandoned the original objectives for single x-ray pulse, dual detector mammography and are focussing on a dual x-ray pulse, single detector system approach. The primary motivation for this change was based on poor DQE results of the rear CCD detector system in the original sandwich design. Also, an amorphous silicon thin film transistor x-ray detector system became available in the principal investigator's laboratory as a result of other research agreements. This technology is available for this research at no cost to this grant. Monte Carlo studies have been completed which assess the dose to the breast at higher energies, and these data were necessary for the optimization studies now underway. Dual-energy mammography remains promising, especially with digital systems nearing the marketplace. The potential of the dual energy examination should be well understood at the end of this coming year.</p>		
14. SUBJECT TERMS  Breast Cancer					15. NUMBER OF PAGES 51	
					16. PRICE CODE	
17. SECURITY CLASSIFICATION OF REPORT  Unclassified		18. SECURITY CLASSIFICATION OF THIS PAGE  Unclassified		19. SECURITY CLASSIFICATION OF ABSTRACT  Unclassified		20. LIMITATION OF ABSTRACT  Unlimited

FOREWORD

Opinions, interpretations, conclusions and recommendations are those of the author and are not necessarily endorsed by the U.S. Army.

       Where copyrighted material is quoted, permission has been obtained to use such material.

       Where material from documents designated for limited distribution is quoted, permission has been obtained to use the material.

✓ Citations of commercial organizations and trade names in this report do not constitute an official Department of Army endorsement or approval of the products or services of these organizations.

       In conducting research using animals, the investigator(s) adhered to the "Guide for the Care and Use of Laboratory Animals," prepared by the Committee on Care and use of Laboratory Animals of the Institute of Laboratory Resources, national Research Council (NIH Publication No. 86-23, Revised 1985).

✓ For the protection of human subjects, the investigator(s) adhered to policies of applicable Federal Law 45 CFR 46.

       In conducting research utilizing recombinant DNA technology, the investigator(s) adhered to current guidelines promulgated by the National Institutes of Health.

       In the conduct of research utilizing recombinant DNA, the investigator(s) adhered to the NIH Guidelines for Research Involving Recombinant DNA Molecules.

       In the conduct of research involving hazardous organisms, the investigator(s) adhered to the CDC-NIH Guide for Biosafety in Microbiological and Biomedical Laboratories.

  
PI - Signature

3 SEPT 98

Date

# Single-pulse dual-energy mammography using a binary screen coupled to dual CCD cameras

U.S. Army Grant DAMD17-94-J-4424  
Principal Investigator: John M. Boone, Ph.D.

Annual Report for 1997-1998

## TABLE OF CONTENTS

<b>Introduction</b>	.....	2
<b>Body of Report</b>	.....	4
Monte Carlo Simulations: DgN		
Calculations	.....	4
Single Energy Mammography Optimization	.....	21
Study of X-ray Fluorescent Reabsorption	.....	25
Breast Phantom Development	.....	32
Detector Description and Configuration	.....	35
Detector Analysis	.....	39
Dual Energy Images	.....	41
<b>Conclusions</b>	.....	45
<b>References</b>	.....	47

## INTRODUCTION

This is the fourth annual report for this four-year grant, however a one-year no cost extension to the grant was requested and approved. Therefore, this is not the final report of the grant activity but is rather a description of the progress towards the grant's objectives made over the past year.

The PI has spent considerable effort in developing Monte Carlo simulation code for the evaluation of dose deposition in the breast during x-ray procedures. This research was mandated by the fact that current roentgen to rad conversion factors in the literature do not address the high energies required for dual energy imaging of the breast. After meeting with considerable difficulty in obtaining results comparable to previously published data (principally from the work of Wu, Barnes and Tucker), the development of custom code was abandoned and existing mature Monte Carlo code (TART 97) was obtained from Oak Ridge National Laboratories. After several months of becoming familiar with the TART 97 series of programs, it became clear that the PI's previous results were in fact equivalent to the TART 97 output. Having renewed confidence in the validity of the Monte Carlo simulation data, the PI expanded his literature search. As a result of reading and re-reading several articles in the literature describing the calculation of glandular dose from Monte Carlo studies, it was realized that other investigators used a simple recalibration procedure that the PI had not previously considered. After implementing this correction, excellent agreement was achieved between the Dgn values computed and those found in the literature. The procedures used, and the new results obtained in this research, are described in this report.

The development and optimization of dual energy mammography techniques requires a realistic breast phantom for experimental studies. Whereas there are many breast phantoms available commercially for single energy mammography and for routine quality assurance, the requirements of a phantom suitable for dual energy mammography research are significantly more severe. In this report, efforts to produce a realistic dual energy suitable, mixed composition (adipose and glandular) breast phantoms are described.

The original goals of producing a dual energy detector system for mammography were focused on single pulsed x-ray acquisition model. The original goals, developed in 1993, also were based upon the use of dual CCD cameras for the digital mammographic acquisition. Several years of studying this detector geometry experimentally, coupled with recent developments in detector technology, has led us to abandon our original objectives for single x-ray pulse, dual detector mammography. Instead, a dual x-ray pulse, single detector system approach has been adopted. The primary motivation for this significant change in design objectives was based on DQE analysis of the rear detector system in the sandwich design. It was realized, and then fully appreciated in quantitative terms, that the tradeoffs in sandwich detector systems for dual energy acquisition were grim; while increased energy separation could be achieved by increasing the thickness of the front detector and inter-detector filter, gains main in energy separation simultaneously

worsened the DQE performance of the rear detector. An amorphous silicon thin film transistor x-ray detector system became available in the principal investigator's laboratory as a result of other research agreements. This technology therefore is available for the present research at no cost to this grant.

The change in the design paradigm from single x-ray pulse/dual sandwich detectors to dual x-ray pulse/single x-ray detector solves the problems associated with the sandwich detector, however the burden is then shifted to developing an x-ray system capable of very rapid energy switching and pulsing. Coincidentally, co-investigator Tony Seibert has been studying, with Robert Alvarez, the efficacy of dual kV pulsed dual energy mammography (1). Dr. Seibert's research, being conducted in the same x-ray labs as this project, has led to the development of very fast x-ray switching procedures for the constant potential generator in our laboratory. Presently, through computer control Seibert and Alvarez have engineered dual kV x-ray pulses (56 and 120 kV) separated in time by approximately 30 msec. After watching that technology progress, it became clear that a 30 msec time delay in x-ray pulses for the dual energy mammography project was quite acceptable considering the aggressive compression techniques used in mammography. The dual x-ray pulsed approach, therefore, appears highly plausible in the context of dual energy mammography and this information was useful in making the decision to go to the dual x-ray pulse/single detector design for the dual energy mammography system. While it is true with current technology that 30 msec readout on the amorphous silicon TFT is currently not feasible on the Varian system at full resolution, 30 frame per second acquisition (33 msec readout time) is possible by binning 2 x 2 pixels. It was therefore also felt that real time detector readout using amorphous silicon TFT technology is but months or years away, which makes the dual energy mammography system based on this technology quite feasible as well.

## BODY OF REPORT

### Monte Carlo Simulations: DgN Calculations

The assessment of radiation dose to the breast during mammography has been of interest to many investigators(2-20). Over the years, the normalized glandular dose (DgN) has come to serve as the benchmark parameter useful for calculating the glandular dose in clinical mammography procedures. The DgN values are essentially the “Roentgen to Rad” conversion values, calculated for the “at risk” glandular component of the breast. Recent efforts to calculate DgN tables for the mammography community have focused primarily on clinically relevant spectra(5,8), using Mo/Mo, Mo/Rh, or Rh/Rh as anode/filter combinations in the 20 kV to 35 kV range.

This work was intended to extend the utility of DgN calculations to higher x-ray energies (up to 120 keV), and to provide the tools for investigators to calculate DgN values for arbitrary x-ray spectra, including monoenergetic x-ray beams in dual energy mammography, where the optimal high energy beam is likely to be very high (>100 keV), well beyond current clinical x-ray mammography beam energies. In addition, with the recent introduction of full field digital mammography systems into the clinical environment, it is likely that slightly higher energy x-ray beams may become useful under some instances.

This work was also intended to extend DgN tables towards thicker breasts, and values reported here are provided for breast thicknesses from 2 cm to 12 cm in 1 cm increments. While the typical compressed breast thickness in the United States is approximately 4.2 cm, there are many women with compressed breast thicknesses ranging to 12 cm and greater.

#### **Methods and Materials:**

##### **Details of the Monte Carlo Study**

Monte Carlo procedures were used to compute the glandular dose to the breast. While the author has developed independent computer code for Monte Carlo studies(21,22), the TART97 Monte Carlo code was purchased from Oak Ridge National Laboratory for use in this study. The TART97 code was developed primarily at Lawrence Livermore National Laboratory(23,24), and is a thoroughly verified and mature Monte Carlo program. A full description of the TART97 Monte Carlo program is left to references, however a brief description is appropriate here. TART97 uses multiple scattering calculations, and follows the history of all photons including photoelectric characteristic emissions (this feature was enabled), and includes the photoelectric, Rayleigh, and Compton scatter interaction mechanisms in the energy region reported. All photons were followed until they either left the volume of interest, were completely absorbed, or reached an arbitrarily small energy (0.10 keV). The TART97 Monte Carlo package utilizes a script language for the input of all parameters, and in particular it has

the ability to specify very detailed and complicated simulation geometry involving the source, patient, and detector.

Monoenergetic x-ray photons at 1 keV intervals were input into each of the simulation runs. Each photon run made use of one million photons at each monoenergetic energy, and these data were used to construct monoenergetic  $D_{gN}$  tables in a procedure described below. The lowest energy simulated was 1 keV, and the highest was 120 keV. For the polyenergetic spectra reported, weighted sums of the monoenergetic  $D_{gN}$  tables were computed. The x-ray spectra used for this study were generated using the “TASMIP” and “MASMIP” models reported previously(25,26). The x-ray coefficients for the filters were also reported previously(27).

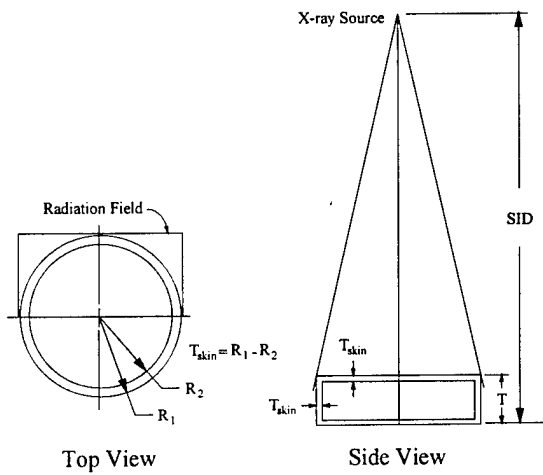


**Figure 1:** The geometry that was used for the Monte Carlo simulations is shown. Geometrical terms used in the text are also defined.

#### Geometry and Composition Issues

The geometry simulated in this study is shown in Figure 1. Instead of using a “D” shaped semicircular breast shape as others have used, a cylindrical breast shape was simulated as shown in Figure 1. The cone-shaped radiation field emitted from the source was collimated to irradiate half of the breast (a semicircle). The semicircular field geometry was particularly simple to simulate using the TART97 code, and efficient to run. The semicircle of breast tissue that was not in the radiation field was intended to simulate the presence of the torso of the patient (the chest wall). The presence of tissue outside of the radiation field may have a minor influence in terms of backscatter, and this is of particular concern in this study due to the much higher x-ray energies studied here. While the non-irradiated semicircle is not the exact geometry of the chest wall, it was thought that the presence of some tissue behind the breast is slightly more representative of that in mammography, rather than having no tissue outside of the radiation field.

Various breast compositions were studied, from 0% glandular/100% adipose to 100% glandular/0% adipose. For concise reference henceforward, the breast composition

will be referred to in terms of the glandular percentage only. The compositional data from Hammerstein were used(28). X-ray coefficients for compound (multi-elemental) substances such as breast tissue are prorated based on the weight fraction of the element; however in substances where the density changes with the composition there are some nuances to consider.

For a tissue containing a weight fraction  $f_g$  of glandular tissue (and correspondingly a weight fraction  $(1-f_g)$  for adipose tissue), and it can be shown that the glandular volume fraction,  $v_g$ , is given by:

$$v_g = \left\{ \frac{(1 - f_g)}{f_g} \frac{\rho_g}{\rho_a} + 1 \right\}^{-1} \quad (1)$$

Where  $\rho_g$  is the density of 100% glandular tissue ( $\rho_g = 1.04 \text{ g/cm}^3$  from Hammerstein) and  $\rho_a$  is the density of 100% adipose tissue ( $\rho_a = 0.93 \text{ g/cm}^3$ ). Letting the total volume be set to unit volume ( $1 \text{ cm}^3$ ) for simplicity, such that  $v_g + v_a = 1 \text{ cm}^3$ , the compound density is:

$$\rho_{\text{compound}} = \rho_g v_g + \rho_a v_a \quad (2)$$

The mass  $m$  of each component in the unit volume is simply  $m_g = \rho_g v_g$  and  $m_a = \rho_a v_a$ , where the “g” subscripts refer to glandular tissue and the “a” subscripts refer to adipose tissue. Using the above procedure, the linear attenuation coefficients for 0%, 50%, and 100% glandular tissues were compared to those reported by Hammerstein. These data are shown in Figure 2.

The breast tissue (glandular and adipose compound) is enclosed in a layer of skin, as illustrated in Figure 1. The skin thickness was varied in this study. For comparison with the results of Dance(6), a skin thickness ( $T_{\text{skin}}$  in Figure 1) of 5 mm was used. For comparison with the results of Wu, Barnes and Tucker(5), a 4 mm skin thickness was used. For one geometry and breast composition, the influence of skin thickness from 2 mm to 6 mm was studied.

#### Conversion of Monte Carlo Results to DgN values

For a given breast composition, photon energy, and geometry, the output produced by the TART97 Monte Carlo package of interest in this study is the energy deposited (normalized per input photon) in the breast tissue compartment (see Figure 1). The average energy to the breast tissue compartment, per incident x-ray photon to the breast, was normalized by the energy of the incident photons (all Monte Carlo runs used monoenergetic spectra), such that the fractional energy absorption,  $f(E)$ , was calculated:

$$f(E) = \frac{\text{energy absorbed per incident photon}}{\text{photon energy}} \quad (3)$$

For  $E$  expressed in the units of keV, and with an x-ray photon spectra,  $\Phi(E)$ , normalized(26) to the number of photons corresponding to 1 Roentgen (for the entire spectrum),  $D_{gN}$  values were calculated using:

$$D_{gN} = \sum_{E=E_{\min}}^{E_{\max}} f(E) E \left(1.6021 \times 10^{-8}\right) \Phi(E) G \frac{\text{area}}{\text{mass}} \quad (4)$$

Where the value of  $f(E)$  is defined in Equation 3, the constant corrects for various unit conversions,  $G$  is defined below in Equation 6, **area** is the surface area of the breast exposed to x-rays, and **mass** is the mass of the purely glandular portion of the breast tissue. Let  $f_g$  be the glandular fraction, by weight, of the breast tissue. For example,  $f_g=1.0$  for a 100% glandular breast, and  $f_g=0.5$  for a 50% glandular breast. For a semicircular breast tissue compartment of radius  $R_2$  (see Figure 1), a breast density  $\rho$ , a compressed breast of thickness  $T$ , a skin layer of thickness  $T_{\text{skin}}$ , the **mass** term in Equation 4 is given by:

$$\text{mass} = f_g \frac{1}{2} \pi R_2^2 (T - 2T_{\text{skin}}) \rho \quad (5)$$

The  $G$  term in Equation 4 corrects the normalized dose calculation specifically to the glandular component of the breast tissue ( $D_{gN}$ ), in a heterogeneous tissue matrix. Breasts with a 0% glandular fraction are computed by extrapolation from  $D_{gN}$  calculations of glandular fractions in the 2%-5% range.

$$G = \frac{f_g \left( \frac{\mu_{en}}{\rho} \right)_g}{\left[ f_g \left( \frac{\mu_{en}}{\rho} \right)_g + (1 - f_g) \left( \frac{\mu_{en}}{\rho} \right)_a \right]} \quad (6)$$

where the mass energy absorption coefficients,  $(\mu_{en}/\rho)$ , for adipose tissue is specified with an "a" subscript and for glandular tissue with a "g" subscript. The deduction of the above equations from previous references(5,6) was not completely obvious to the PI, and therefore an attempt is made here to explicitly state the calculations involved in developing the  $D_{gN}$  for this study. For further clarification, the units of the variables used in Equation 4 are indicated below:

Term in Equation 4	Units
$D_{gN}$	milliRads / Roentgen
$f(E)$	unitless
$E$	keV/photon
$\Phi(E)$	photons/mm <sup>2</sup> /R
$G$	unitless
<i>area</i>	mm <sup>2</sup>
<i>mass</i>	grams (g)
$1.6021 \times 10^{-8}$	mRad g / keV

The constant  $1.6021 \times 10^{-8}$  is derived below:

$$(1.6021 \times 10^{-8}) \frac{(mRad \ g)}{(keV)} = (1.6021 \times 10^{-9}) \frac{ergs}{keV} \times \frac{1000 \ mRads}{Rad} \times \frac{g \ Rad}{100 \ ergs}$$

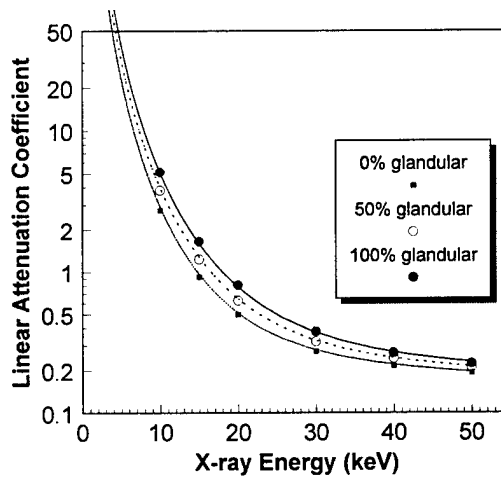


**Figure 2:** The linear attenuation coefficients computed in this study (lines) are compared with the data reported by Hammerstein(28), for 0%, 50%, and 100% glandular tissue. Excellent agreement in terms of the attenuation coefficients is observed over the energy range compared.

## Results:

### Monte Carlo Results, $f(E)$

The Monte Carlo results for 0%, 50%, and 100% glandular breasts are illustrated in Figure 3A, 3B, and 3C, respectively. The absorbed fraction of the incident energy fluence,  $f(E)$ , is shown for monoenergetic x-ray photons from 1 to 120 keV. These plots were computed using 1 keV spacing. The data for the 2 cm breast are illustrated as the bottom curve on Figures 3A-C, and the data for the 12 cm breast are shown on the top curve. Intermediate curves correspond to 3, 4, 5, ..., 9, 10, 11 cm data (from the bottom up), and curves showing odd-numbered thicknesses are dashed. The shape of the 11 curves in each of the Figures (3A, 3B, and 3C) is of interest. If the breast tissue was not encapsulated in a layer of skin, these curves would be pseudo-exponential,  $f(E)$  being unity at the very low energies, decreasing almost exponentially with increasing energy. However, the lowest energy x-ray photons are unable to penetrate the relatively thin skin layer to contribute a fraction of their energy to the breast tissues; rather, the energy is deposited in the skin layer. The value of  $f(E)$  is therefore substantially damped at the low energies by the skin filtration effect.

As the glandular fraction increases (Figures 3A→3C), the fractional absorption  $f(E)$  of the incident x-rays increases slightly, as would be expected due to the changing composition and increasing density. It is instructive to plot the data illustrated in Figure 3 differently, essentially slicing the family of curves in a different dimension. For example, Figure 4 illustrates  $f(E)$  as a function of breast thickness for a family of curves at different energies for a 50% glandular breast. The absorption of 10 keV photons is constant across breast thicknesses, suggesting that the absorption dynamics of these low energy photons occurs in the first 2 cm of tissue. At higher incident photon energies, the fractional energy absorption,  $f(E)$ , increases with increasing breast thickness, as would be expected. Figure 5 demonstrates yet a different perspective of this data, showing  $f(E)$  as a function of glandular fraction for different incident photon energies for a 4 cm breast. Monte Carlo runs were performed at several intermediate glandular fractions (0%, 20%, 40%, 50%, 60%, 80% and 100%) for this figure, as shown as data points on Figure 5. The curves shown in Figure 4,  $f(E)$  versus breast thickness, are non-linear, whereas the curves in Figure 5,  $f(E)$  versus glandular fraction, are quite linear. This observation suggests that linear interpolation between glandular fraction data, for the  $f(E)$  data, is reasonable and preferable over interpolating between breast thicknesses.

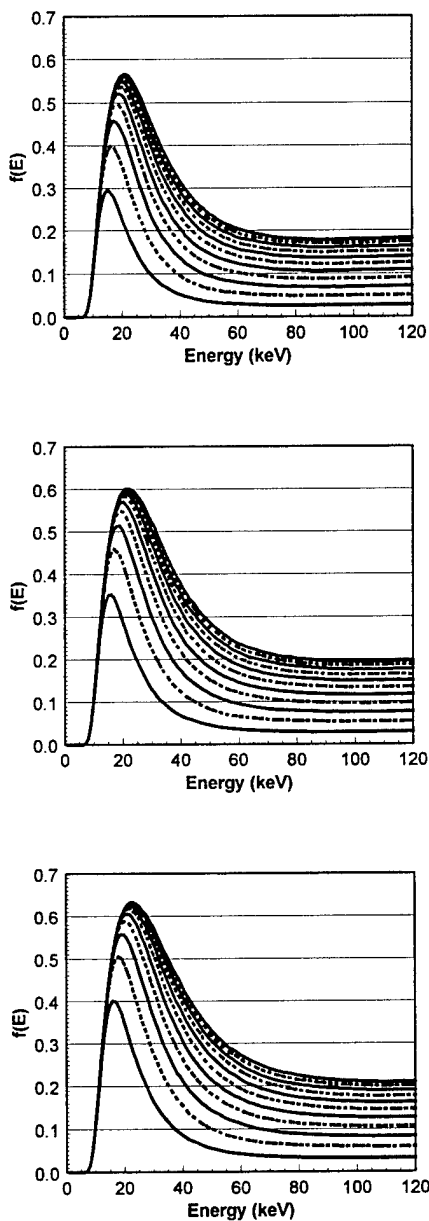


**Figure 3:** The fraction of absorbed energy in the breast tissue per photon,  $f(E)$ , as a function of incident x-ray energy is illustrated for 0% glandular tissue (top), 50% glandular tissue (middle), and 100% glandular tissue (bottom). The  $f(E)$  curves are shown for 11 tissue thicknesses ranging from 2 cm to 12 cm, in 1 cm increments. The bottom curve on each graph represents the data for the 2 cm breast thickness, and the top curve shows the  $f(E)$  curve for the 12 cm thick breast. Intermediate curves run in order from 2 to 12 cm. The odd-numbered tissue thicknesses (e.g. 3 cm, 5 cm, ... 11 cm) are illustrated using dashed lines, while the even-numbered thicknesses are shown as solid lines. The  $f(E)$  values are low at the lowest incident x-ray energies due to the filtration effect of the skin layer.

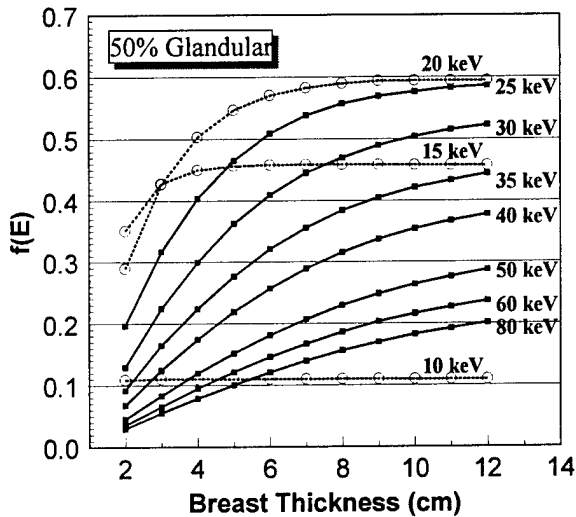


**Figure 4.** The data shown in Figure 3 is replotted here illustrating a different perspective of the  $f(E)$  data. At 10 keV,  $f(E)$  is almost constant as a function of breast thicknesses. The fact that the 10 keV photon absorption fraction is non-zero implies that 10 keV photons penetrate the skin layer, but its constant behavior as a function of breast thicknesses implies that the absorption kinetics take place principally in the first 2 cm of the breast. Higher energy photons show increased penetration of the skin layer ( $f(E)$  values are higher for the 2 cm breast), and also demonstrate that increased tissue absorption occurs with thicker breasts, as would be expected

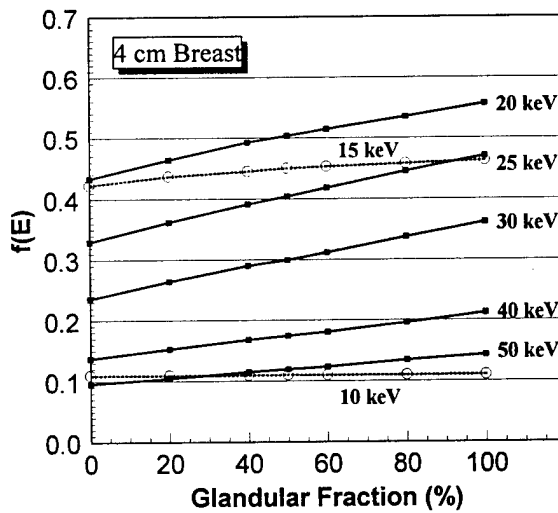


**Figure 5:** This figure illustrates, for a 4 cm breast, the absorption fraction  $f(E)$  as a function of glandular fraction, for various x-ray energies. The absorption is nearly a linear function of glandular fraction, as evidenced by the linearity of the curves.

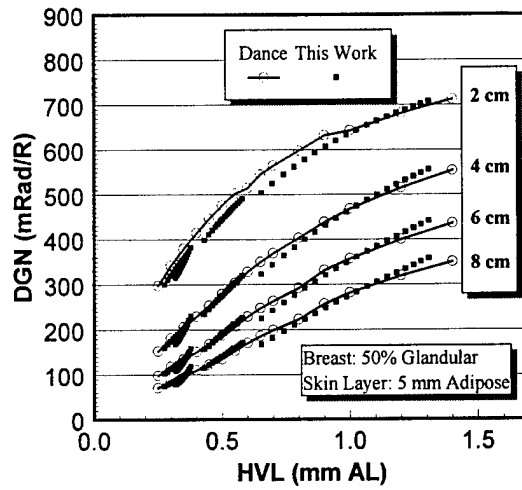


**Figure 6:** The DgN values computed by Dance(6) are compared against the DgN values generated in this study, for breast thicknesses of 2, 4, 6, and 8 cm. Dance reported DgN values as a function of the HVL of the x-ray beam, and that approach was adopted here as well. Good qualitative comparison is seen.

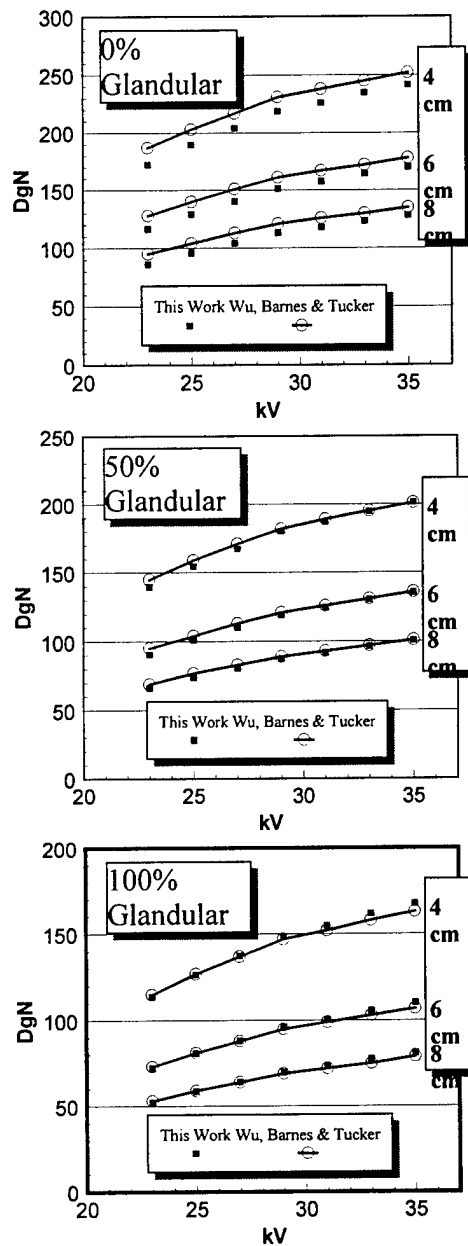


**Figure 7:** The DgN values reported by Wu, Barnes, and Tucker (WBT) (5) are compared with the DgN values computed here. The DgN values for a 0% glandular breast are shown (top), for a 50% glandular breast are shown in the middle plot, and the data for a 100% glandular breast is shown on the bottom figure. The DgN values reported here, averaged over all kV's and breast thicknesses, differed from the WBT DgN values by -6.2% for the 0% glandular breasts, -1.9% for the 50% glandular breast, and +0.9% for the 100% glandular breasts.

### Comparison to the D<sub>gN</sub> values of Others

D<sub>gN</sub> values computed here were compared against the work of Dance(6), as illustrated in Figure 6. Dance presented his conversion factors in different units (mean glandular dose per incident air kerma, mGy/mGy), which were recomputed to the units of mRad/R for this comparison. For this comparison, the skin thickness was set to 5 mm, and a 50% glandular breast was modeled consistent with Dance's methods. Four different breast thicknesses, 2, 4, 6 and 8 cm were studied for this comparison.

Considering the different Monte Carlo routines, and particularly the different x-ray spectra used to produce this data, the qualitative agreement seen in Figure 6 between the Dance data and this work is quite good. The 4 cm data was subjected to quantitative comparison. Because the HVL's corresponding to both data sets differed on a point by point basis, direct comparisons between the data sets were not possible. Therefore, both data sets were computer fit using commercially available software (TableCurve 3.0, Jandel Scientific, Corta Madera, CA) with excellent precision (Dance 4 cm data set,  $r^2=0.9999$ , 4 cm data reported here,  $r^2 = 0.9975$ ), and comparison was then made between the computer fit D<sub>gN</sub> values (between data sets) over the range of 0.25 mm Al HVL to 1.3 mm Al HVL. The 4 cm data reported here was found to differ by -1.12% compared to Dance's, with a standard deviation of 2.66%. In terms of absolute D<sub>gN</sub> values, the difference was -3.34 ( $\sigma=10.6$ ) mRad/R.

The data of Wu, Barnes, and Tucker (WBT)(5) are the most commonly used D<sub>gN</sub> values in the United States, and comparison is made with the WBT data in Figure 7A for the 0% glandular breast, in Figure 7B for the 50% glandular breast, and in 7C for the 100% glandular breast. D<sub>gN</sub> values calculated at three breast thicknesses (4, 6 and 8 cm) are shown in Figures 7A-C. The D<sub>gN</sub> values produced in this study were consistently but only slightly lower than the WBT values for the 0% glandular breast, but were seen to be in excellent agreement with the WBT data for the 50% and 100% glandular breast compositions. The slight qualitative differences (5-7%) with the 0% glandular data (Figure 7A) may be a consequence of different extrapolation techniques to the 0% glandular breast. The spectra computed for this study were hardened by adding plexiglass such that the half value layers (HVLs) matched exactly those reported by WBT. The D<sub>gN</sub> values calculated in this study, did however make use of a different spectral model(25) than that of WBT(29), and this may explain the slight differences between the D<sub>gN</sub> values derived here and those of WBT.

The D<sub>gN</sub> values calculated in this work were calculated at exactly the same HVL that the WBT D<sub>gN</sub> values were reported at, and thus a direct comparison between the WBT D<sub>gN</sub> values and those reported here is possible. For the 0% glandular data, the mean differences (and standard deviations) averaged over the 7 spectra (kV=23, 25, ...35) are -5.5% (1.3%) for 4 cm, -6.3% (1.7%) for 6 cm, and -6.8% (1.5%) for the 8 cm breast thickness. For the 50% glandular breast, the mean ( $\sigma$ ) differences were -1.5% (1.4%), -1.9% (1.5%), and -2.3% (1.6%) for the 4, 6 and 8 cm breasts, respectively. For the 100% glandular breast, the differences between the D<sub>gN</sub> values reported here and the

WBT values were 0.6% (1.5%), 1.0% (1.4%) and 1.1% (1.7%) for the 4, 6 and 8 cm breast thicknesses, respectively.

#### Influence of Skin Thickness

The calculation of glandular dose for a patient has a large number of uncertainties associated with it, and estimating cancer risk from the glandular dose has even greater uncertainties. The uncertainties in calculating glandular dose include uncertainties in the tabulated  $D_{gN}$  values, but also practical uncertainties in assessing the thickness of the breast, the breast composition, the precise mAS used, differences between the actual mammography geometry and that used in Monte Carlo simulations, and so on. Figures 3A-C illustrate that the highest fractional energy absorption of incident x-ray photons occurs in the energy region from about 15 keV to 25 keV, where the peaks of the  $f(E)$  curves are. Not coincidentally, this is the energy region where the vast majority of the x-ray photons in conventional x-ray spectra (e.g. Mo/Mo 26 kVp) exist. The fact that there is high breast absorption in this energy region also suggests that photons in this energy range are useful in producing high contrast images. As mentioned previously, the left edges of the  $f(E)$  peaks seen in Figures 3A-C are a consequence of the absorption of incident x-rays by the skin layer. The slope of the left edges of the  $f(E)$  peaks suggests that small differences in the assumption of skin thickness may have a large influence on the overall accuracy of the dose calculation. To examine this in the case of the typical breast, Monte Carlo studies were performed using different skin thicknesses. Figure 8 illustrates the calculated  $D_{gN}$  values for a 50% glandular, 4 cm breast. The data of WBT (using a 4 mm skin thickness) are shown as the solid circles, and the  $D_{gN}$  values computed here for skin thicknesses from 2 mm to 6 mm are also shown in Figure 8. Averaged over the different x-ray spectra, the change in  $D_{gN}$  values (relative to a 4 mm skin thickness) resulting from different skin thicknesses is +15.2% ( $\sigma=2.1\%$ ) for a 2 mm skin layer, +7.1% (0.9%) for a 3 mm skin thickness, -6.4% (0.7%) for 5 mm skin, and -11.8% (1.3%) for a 6 mm skin thickness.

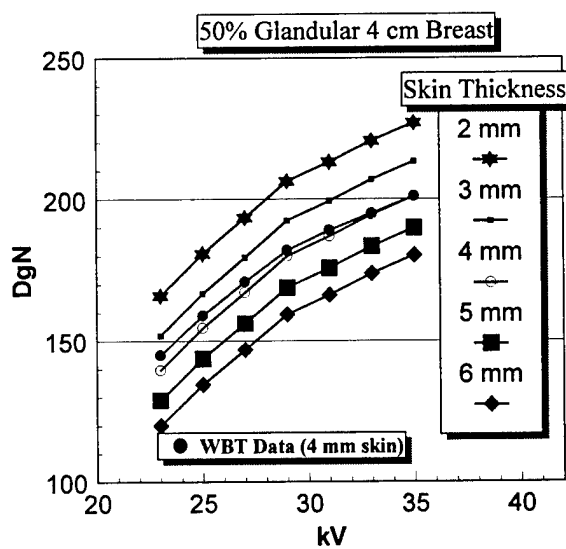


Figure 8:

This figure illustrates the influence that the thickness of the skin has on the  $D_{gN}$  value. Compared to the 4 mm skin thickness used by WBT (their data shown as solid circles), the  $D_{gN}$  values on average increased +7% for a 3 mm skin layer, and +15% for a 2 mm skin layer. The  $D_{gN}$  values decreased by -6% and -12% for skin layers of 5 and 6 mm, respectively.

The observation that the skin thickness has a large influence on the  $D_{gN}$  value is not surprising given the shape of the absorption curves (Figures 3A-C). The purpose for presenting these data is, however, to demonstrate that of the uncertainties involved in dose calculations, it is likely that the slight differences (<6%) in tabulated  $D_{gN}$  values produced by different investigators are *quite* small compared to the large errors that can be made in making the wrong assumptions or generalizations about an individual patient's breast characteristics.

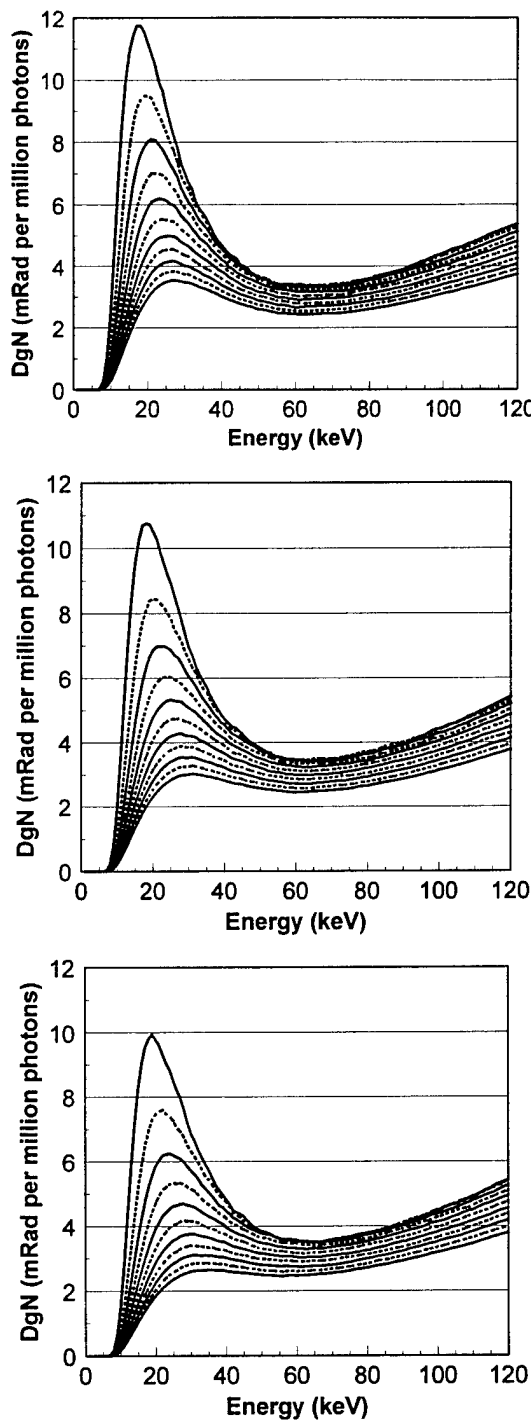
#### Monoenergetic Results

Figure 9 illustrates the monoenergetic  $D_{gN}$  values in the units of mRad per  $10^6$  photons per energy interval. Figures 9A, 9B, and 9C correspond to the 0%, 50%, and 100% glandular fractions. While the general shape of these curves is similar to the  $f(E)$  curves shown in Figure 3, the influence of tissue thickness is inverted.  $D_{gN}$  values for the same energy and breast composition increase with decreasing breast thickness, because there is less self shielding in the thinner breast. While the  $D_{gN}$  values are high for thinner breasts, the entrance exposure during a mammogram is markedly lower in thin breasts, and therefore thin breasts typically receive substantially lower glandular doses than breasts of greater thicknesses. An alternate ordinate axis label for Figure 9 would be  $D_{gn}$  ( $\times 10^{-6}$ ) per photon, or  $D_{gN}(E)$ . Therefore, by multiplying the data in the figure by  $10^{-6}$ , and then integrating the product of an incident x-ray spectrum ( $\Phi(E)$ ) and the appropriate curve in Figure 9 ( $D_{gN}(E)$ ), the  $D_{gN}$  value for an arbitrary spectrum can be calculated, as shown below:

$$DgN = \sum_{E=E_{\min}}^{E_{\max}} D_{gN}(E) \quad (10^{-6}) \quad \Phi(E) \quad (8)$$

where it is understood that the total number of photons in  $\Phi(E)$  above in Equation 8 is normalized to 1 Roentgen. The curves shown in Figure 9, coupled with the formula shown in Equation 8, are most useful when dealing with an arbitrary x-ray spectrum, which is typically computed in the units of photons/mm<sup>2</sup>/per energy bin.

Photons at different energies contribute differently to exposure in air, due to the energy dependence of the mass energy attenuation coefficient of air. Consequently,  $D_{gN}$  values expressed in the traditional units of mRad per R as a function of E (Figure 10) have a different shape than the  $D_{gN}$  per photon curves shown in Figure 9. Figures 10A and 10B illustrate the mRad/R  $D_{gN}$  values for 0% and 100% glandular tissue, respectively. Figure 10 is directly useful if one is interested in the  $D_{gN}$  value for a monoenergetic beam of 1 R incident exposure to the breast.



**Figure 9:** DgN normalized

values are glandular dose

values, but in this figure the DgN values are normalized per entrant photon instead of per Roentgen as is more typical. The DgN values are shown for 0%, 50% and 100% glandular breasts in Figures 9A, 9B, and 9C respectively. Curves are shown for thicknesses ranging from 2 cm to 12 cm by 1 cm increments, but only the two end thicknesses are illustrated. The DgN values shown here are higher for thin breasts and lower for thicker breasts, reversing the trend seen for fractional energy absorption  $f(E)$  seen in Figures 3A, 3B, and 3C. This figure illustrates that on a *per photon* basis, photons in the energy region between approximately 12 keV and 30 keV contribute the most to the normalized glandular dose, and of course this is the energy region where most conventional mammographic x-ray spectra are centered.

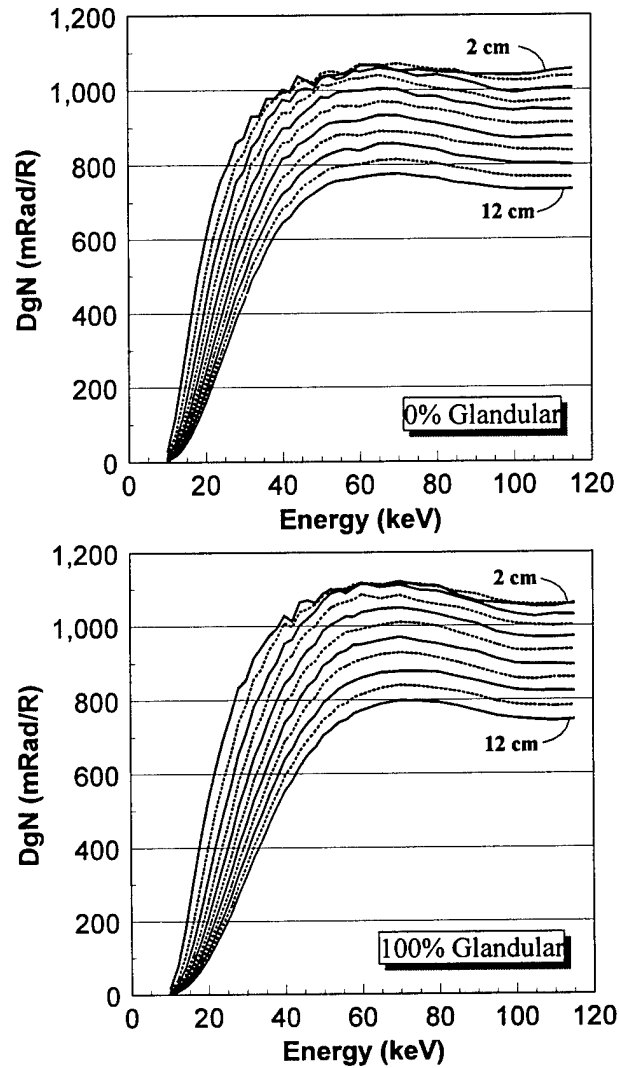


**Figure 10:** The DgN values for monoenergetic x-ray energies are shown, in Figure 10A for 0% glandular breasts and in Figure 10B for 100% glandular breasts. The DgN values shown in these graphs are plotted in the conventional units of mRad/R, as opposed to mRad/photon as shown in Figure 9. The curves in this figure can be read directly when assessing DgN for monoenergetic beams

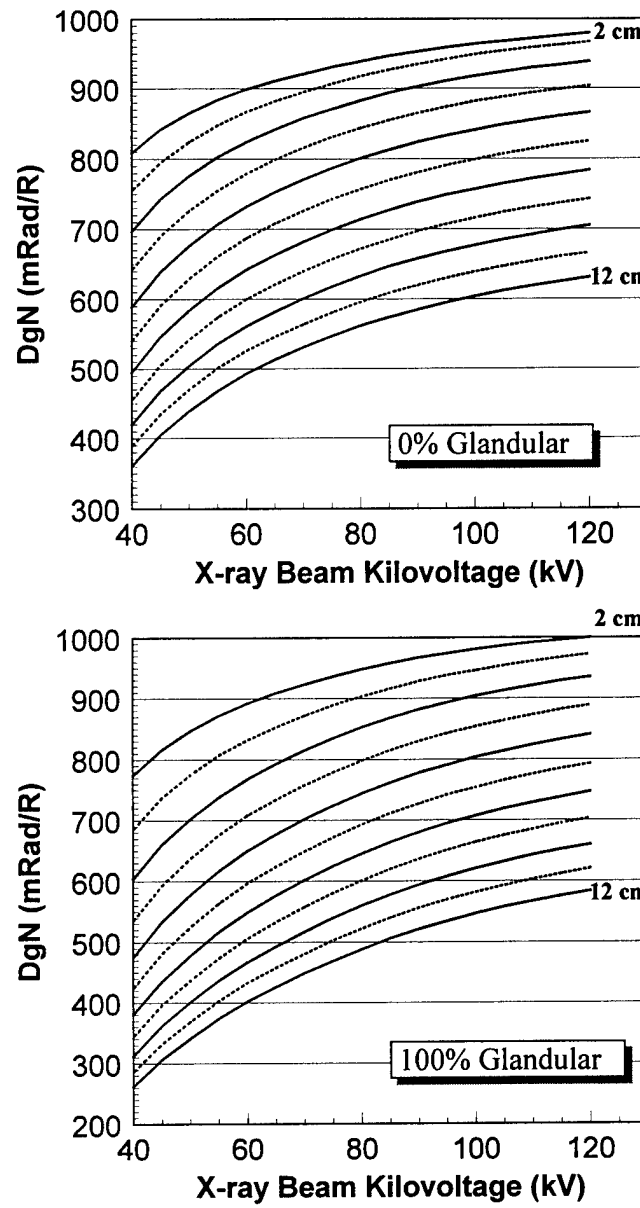


**Figure 11:** D<sub>gN</sub> values are shown for conventional polyenergetic x-ray beams using a tungsten anode and 2.5 mm of added aluminum filtration. D<sub>gN</sub> values for 0% glandular breasts (Figure 11A) and 100% glandular breasts (Figure 11B) are illustrated.

### High Energy Polyenergetic Results

Figure 11 illustrates the  $D_{gN}$  values for polyenergetic x-ray beams in the general diagnostic energy region. Figure 11A shows results for the 0% glandular breast, and Figure 11B shows results for the 100% glandular breast. The x-ray spectra used for these calculations were generated using a spectral model developed by the author(30). The x-ray spectrum was simulated from 40 kV to 120 kV, for an x-ray system with a general diagnostic tube incorporating a tungsten anode, 5% kV ripple (approximating an inverter generator), and with 2.5 mm of added Al filtration. The HVLs ranged from 1.6 mm Al at 40 kV to 5.0 mm Al at 120 kV, with an approximately linear relationship ( $r^2=0.998$ ) between the HVL and kV, where  $kV = 23.318 \text{ HVL} - 0.237$ . This relationship can be used to convert HVL values to the kV values on Figure 11A or 11B.

### Discussion:

Monte Carlo techniques were used to calculate  $D_{gN}$  values. As validation of the procedures used here,  $D_{gN}$  values for conventional mammography spectra were compared against the previously published and seminal work of Dance and Wu, Barnes, and Tucker. The comparison with Dance showed agreement within about 1%, and comparisons with the WBT showed agreement within a range of about 1% to 6%, depending upon breast glandularity. The influence of the skin thickness was evaluated (Figure 8), and it was seen that 100  $\mu\text{m}$  of skin has approximately a 7% influence on the  $D_{gN}$  values. Consequently, a relative difference between the  $D_{gN}$  values of WBT and those reported here is less significant than very small differences (0.1 mm) in women's skin thicknesses.

Having verified the results presented here against existing results for conventional x-ray spectra, the methods were used to extend  $D_{gN}$  Monte Carlo calculations to 120 keV. These data may be useful for computing the  $D_{gN}$  values for arbitrary x-ray spectra, including those spectra which may be useful for dual energy mammography in the high energy region.

## Single Energy Mammography Optimization

Optimization of an x-ray imaging procedure is typically performed so that image quality is maximized per unit dose to the patient. In this study, the signal to noise ratio to the detector was fixed, and the contrast of a microcalcification was calculated and the dose to the breast was calculated. The parameter to optimize is the figure of merit (FOM)(31), which is defined as:

$$FOM = \frac{Contrast \times SNR}{\sqrt{DOSE}} \quad (9)$$

For this study, the contrast was calculated by passing a primary x-ray spectrum through the thickness and composition of the breast under study, under two situations: (1) with only skin and tissue (“background”), and (2) with skin, tissue, and a 50  $\mu\text{m}$  microcalcification (“object”). The energy deposited in the 60 mg/cm<sup>2</sup> Gd<sub>2</sub>O<sub>2</sub>S detector simulated was recorded. The contrast is computed as:

$$Contrast = 100 \times \frac{(object - background)}{background} \quad (10)$$

For this preliminary investigation, the influence of scattered radiation or of an anti scatter grid on the contrast calculation was not considered. The influence of scatter on the dose was considered, however. The glandular dose to the breast (in mRad) was calculated using DgN values tabulated per photon, as described in the previous section of this report.

Optimization needs to include the effects of contrast, dose, and signal to noise ratio (SNR). To do this in the context of Equation 9, the SNR was held constant to the detector (and SNR was set to unity in Equation 9). The SNR was held constant by normalizing the signal (energy) deposited in the detector to a fixed value. The signal level chosen corresponded to an incident exposure of 10 mR on the detector (behind the breast). Because in x-ray imaging, SNR  $\propto$  DOSE<sup>2</sup>, by taking the square root of the dose in the denominator of Equation 9 keeps the FOM independent of exposure levels at constant SNR.

The raw data of a typical optimization scheme are illustrated in Figure 12. On that figure, the entrance skin exposure (ESE), glandular dose to the breast (mRad), contrast (%), and the FOM are illustrated. The FOM was computed per Equation 9, and Figure 12 illustrates the influence of the individual parameters and related ones in Equation 9.

The FOM is illustrated as a function of kV in Figure 13. The peak value in each curve corresponds to the optimal kV for those imaging conditions. The FOM values for thinner breasts are much higher than for thicker breasts because of the dose term in the denominator. Figure 13 illustrates 4 curves, but the FOM curves were calculated for all thicknesses ranging from 2 cm to 12 cm. The optimal kV for each breast thickness and for the Mo/Mo anode filter combination studied here is shown in Figure 14. While this

present simulation does not include the effects of x-ray scatter on contrast, it is comforting nonetheless that the optimal kVs as indicated in Figure 14 are very consistent with current clinical practice.

For extremely large or glandular breasts, current x-ray mammography systems such as the General Electric DMR and the Lorad Mark 4 can make use of alternative anode/filter combinations. Figure 15 illustrates the FOM curves versus kV for three different anode/filter combinations: Mo/Mo, Mo/Rh and Rh/Rh. The FOM values for two breast thicknesses are also illustrated in the figure. For the 4 cm breast, the FOM values for each of the anode/filter combinations are tightly clustered together near the peak of the curves, but separate at higher kVs. The optimal kVs and the corresponding FOMs for the 4 cm breast are 27 kV (FOM=0.679), 28 kV (FOM=0.691), and 30 kV (FOM=0.693) for the Mo/Mo, Mo/Rh and Rh/Rh anode/filter combinations, respectively. In this same order, the corresponding values for the 8 cm breast are 29 kV (FOM=0.268), 29 kV (FOM=0.243), and 32 kV (FOM=0.278). The FOM values are quite similar for the 4 cm breast, indicating that the choice in terms of anode/filter combination is somewhat ambiguous. For example, the coefficient of variation in the peak FOM values for the 4 cm breast is 0.90%. For the 8 cm breast, however, the Rh/Rh anode/filter FOM is 12.6% higher than the Mo/Rh value, and it is 25.2% higher than the Mo/Mo value, indicating a strong superiority of the Rh/Rh spectrum for the 8 cm 50% glandular breast.

Optimization studies for mammography are common in the literature, and the results presented above are not particularly surprising. Indeed, the clinical mammography examination is very close to being optimized (at least for screen-film systems) and those well established *ad hoc* techniques serve as at least a qualitative validation of the Monte Carlo based optimization studies.

Our plan is to perform an extensive optimization study for single energy mammography (expanding the parameter count beyond the preliminary studies presented above), and use those results to in part justify and reinforce comprehensive optimization studies on dual energy mammography techniques.

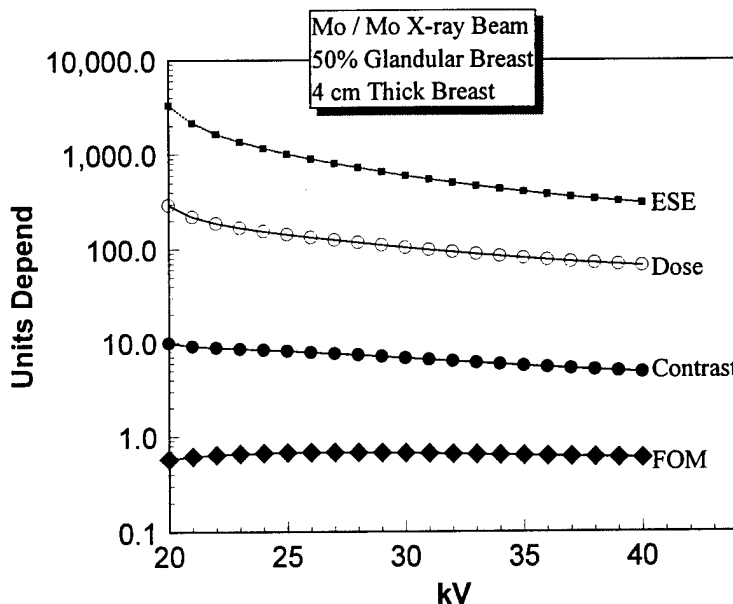


**Figure 12:** The raw data that goes into the calculation of the figure of merit are shown as a function of kV for one breast thickness and composition. The entrance skin exposure (ESE) is shown on top. The dose (mRad) to the breast is computed from the DgN values and the ESE. The contrast (%) is for a 50  $\mu$ m microcalcification. The FOM is calculated as described in the text.

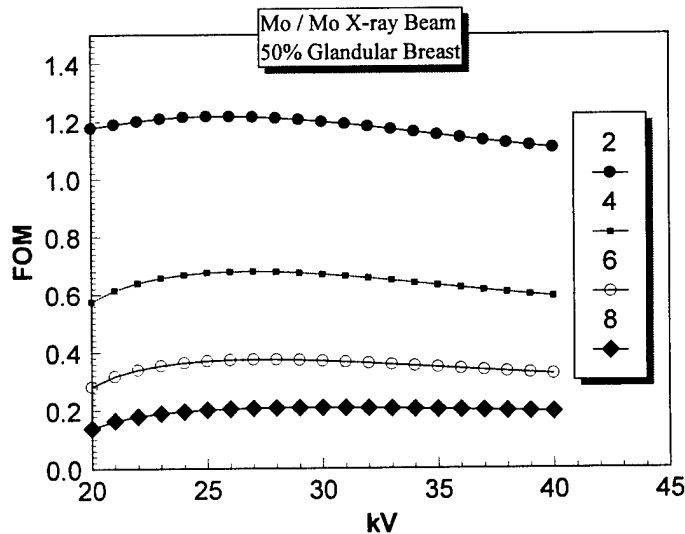


**Figure 13:** The FOM as a function of kV, for 4 different breast thickness (in cm, as indicated on the key). The peak of each curve corresponds to the “optimal” technique for that breast thickness. The absolute values of the FOM are much lower for thicker breasts, reflecting the strong influence that thickness has on increase breast dose.

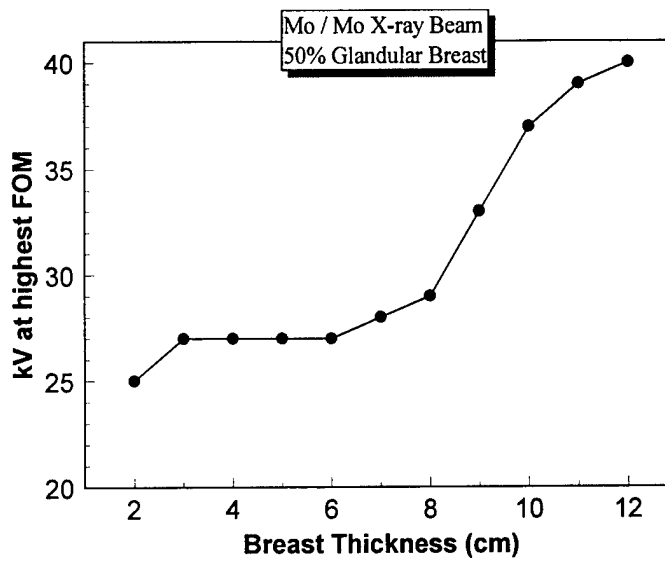


**Figure 14:** The optimal kV as a function of breast thickness for a Mo/Mo anode filter combinations and a 50% glandular breast is shown. Note the “plateau” at 27 kV in the area from 3 cm to 6 cm breasts, encompassing the vast majority of women.

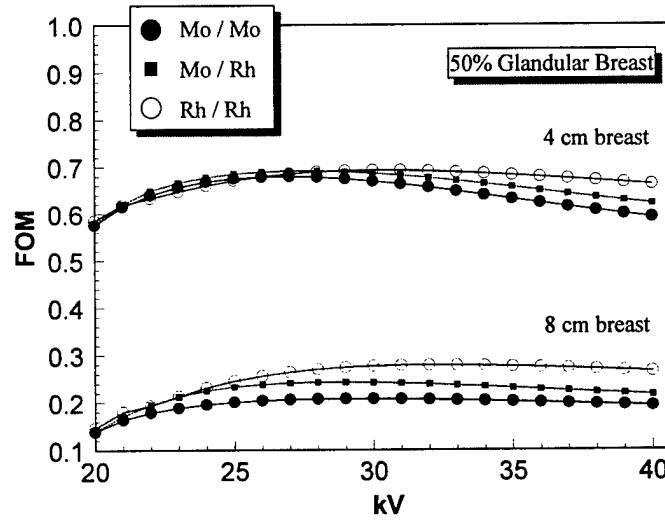


**Figure 15:** The FOM is shown for two different breast thicknesses (4 and 8 cm), and for 3 different anode/filter combinations.

## Study of X-ray Fluorescent Re-absorption

The focus of this grant is on the development of a dual energy detector system for mammography, but underlying this detector system is basically a digital mammography system. There is a great deal of excitement in the field of x-ray detectors, due to the wide variety of digital detector systems nearing pre-market approval and entering the clinical imaging environment. Direct conversion detector systems such as selenium based thin film transistors or lead iodide TFTs have shown exciting potential, as have mosaics of CCD cameras coupled to intensifying screens using miniaturizing fiber optical boules. An amorphous silicon based thin film transistor has been used for this project (the Varian a-Si TFT system is on extensive loan to the PI via an unrelated grant, as discussed in a latter section of this report). For indirect digital x-ray systems, such as the CCD mosaic systems and the a-Si TFT systems, x-ray intensifying screens are required to convert x-ray into light. Unlike in a dual or single emulsion screen-film cassette, however, in a digital system the screen must be positioned with the x-rays striking its front and with the photodetector (e.g. the a-Si TFT) towards the back. To achieve the x-ray absorption of a standard screen-film system ( $\sim 120 \text{ mg/cm}^2$ ), the phosphor coupled to the a-Si TFT system needs to have exceptional absorption properties and be extremely thin due to the light diffusion problems in screens. This new geometry, the constraints it poses on detection efficiency and resolution, and the fact that digital detectors can justify exotic screen technology based upon a relative cost argument, led us to study the x-ray fluorescent reabsorption effects of various phosphors.

For radiographic screen film systems,  $\text{Gd}_2\text{O}_2\text{S}$  is the most commonly used scintillator presently, having replaced  $\text{CaWO}_4$  over two decades ago. While  $\text{Gd}_2\text{O}_2\text{S}$  is an excellent phosphor, a major contributing factor to its success in radiographic screen film systems is its durability and chemical stability. Currently, a wide array of digital radiographic imaging systems are becoming available. Digital radiographic imaging systems, for example those based on amorphous silicon thin film transistor technology, are quite expensive and significantly more fragile than a screen film cassette. Because of the high cost and fragility of the digital electronics with these systems, the x-ray phosphor coupled to them does not need to be as sturdy as in the case of a screen film cassette. This consideration, in part, has led to a renewed search for x-ray phosphors which are most suitable in the digital radiographic environment.

For general diagnostic radiology, screen film systems employ dual-emulsion, dual-screen cassettes. In this design, the x-ray phosphor is essentially sliced into two halves, with the light-detector (the dual-emulsion film) sandwiched between the two halves of the x-ray phosphor screens. This is only possible because x-rays are very efficient at passing through the film base and emulsion. With digital radiographic systems, however, only a single x-ray screen can be used. With these systems, the x-rays are incident upon the x-ray phosphor from the front, while the light sensitive digital receptor (e.g. a-Si TFT) collects the light emitted by the x-ray interactions in the screen behind the screen. Because of this subtle but important change in x-ray detection, the search for x-ray phosphors for digital systems has led to more exotic, more expensive but better performing intensifying screen materials for the digital radiographic application.

The x-ray K edge of an intensifying screen phosphor is an important consideration in the performance of that phosphor for a given diagnostic imaging task. While it is widely assumed that it is desirable to have the majority of the x-ray photons incident upon the intensifying screen with energies above the K edge to improve quantum detection efficiency, the re-emission of characteristic radiation (x-ray fluorescence) will cause loss in the overall absorption efficiency. Worse, when x-ray fluorescence is reabsorbed by the intensifying screen adjacent to the primary x-ray interaction, a loss of spatial resolution and an increase in image noise may occur.

In this study, the influence of x-ray fluorescence on a variety of x-ray intensifying screen phosphors was studied using Monte Carlo techniques. The reabsorption of x-ray fluorescence leads to a redistribution of the incident x-ray energy, as does x-ray scattering within the intensifying screen due to Raleigh and Compton interactions. To isolate the role that x-ray fluorescence plays, Monte Carlo simulations were run using two different modes: the Monte Carlo calculations were run such that x-ray fluorescent energy was assumed to be deposited at the same point as the initial x-ray interaction. A second Monte Carlo run was then executed which tracked the spatial redistribution of x-ray fluorescence energy. By subtracting the data acquired between such runs, the role of Raleigh and Compton scatter could be eliminated. This procedure was used in an analysis of several different possible candidates for x-ray phosphors.  $\text{Gd}_2\text{O}_2\text{S}$ ,  $\text{CsI}$ ,  $\text{Se}$ ,  $\text{YTaO}_4$ , and  $\text{CaWO}_4$ .

This study focuses solely on the Monte Carlo transport of x-ray photons. Obviously, the transport for diffusion of optical photons in an x-ray intensifying screen is an important consideration and in fact may play the predominant role in broadening the point spread function of the screen. However, while x-ray intensifying screens are indirect detectors in which optical energy ultimately stimulates the photo detector, direct detector, direct detectors such as  $\text{Se}$  do not make use of intermediary optical photons but rather the detector reads out the charge (electrons) liberated in the detector by x-ray interaction. Therefore, this study was designed to compare the x-ray scatter and photo electric reabsorption contribution to the point spread function in both direct and indirect x-ray detectors.

## Methods and Materials

Monte Carlo simulations were employed to study the x-ray absorption, scatter, and x-ray fluorescent reabsorption in both direct x-ray detectors (amorphous  $\text{Se}$ ) and common x-ray scintillators. The x-ray phosphors studied were  $\text{Gd}_2\text{O}_2\text{S}$ ,  $\text{CsI}$ ,  $\text{BaFBR}$ ,  $\text{YTaO}_4$ ,  $\text{CaWO}_4$ ,  $\text{ThO}_2$ , and  $\text{Se}$ . The TART 97 Monte Carlo simulation package was used to study the x-ray transport dynamics in this study. TART 97 is a completely verified Monte Carlo set of programs which has a development history spanning several decades. The current generation of this code was developed at Lawrence Livermore National Laboratory (23), and distributed on CD ROM by Oak Ridge National Laboratory (23). The Monte Carlo code uses a script language which allows the user to define relatively complex geometry's, and to specify x-ray source, emission characteristics and arbitrary detector, chemical compositions and densities.

The detector was partitioned into a series of annuli of increasing radius encompassing a center circle where x-ray photons were incident upon the center of the circle at a point. The spacing of the concentric annuli was 0.100 mm extending out to 4.5 mm. For each detector composition and thickness,  $10^7$  x-ray photons were input to the detector at each x-ray energy. X-ray energies ranging from 1.0 keV to 120 keV by 1 keV increments were studied. For each composition, phosphor thickness, and x-ray energy, 2 Monte Carlo runs were initiated each with  $10^7$  photons: one run tracked all scattering (Raleigh and Compton) and x-ray characteristic photons through the phosphor matrix and the surround. A second run tracked all scatter interactions, however x-ray fluorescent photons, when emitted, were considered deposited at the same spatial coordinates as the parent photon. By subtracting the results of these 2 Monte Carlo runs, the influence of only x-ray fluorescent redistribution and reabsorption could be studied independently.

With the exception of the amorphous Se screen, all the other scintillators were considered to be combined with a 5% weight fraction of binder. The elemental composition (C, H, and O) of CarboSET 526 was utilized, as this is a common binder material in the intensifying screen industry. The series of different mass thicknesses ( $\text{mg/cm}^2$ ) from 30  $\text{mg/cm}^2$  to 120  $\text{mg/cm}^2$  by 30  $\text{mg/cm}^2$  intervals. The physical densities indicated in Table 1 were used to adjust the physical thickness of the various x-ray phosphors appropriately. The mass thicknesses reported do not include the contribution of the CarboSET binder, as this is the convention used in the x-ray screen industry.

The x-ray source for each Monte Carlo run consisted of monoenergetic photons normally incident on the x-ray screen. The source to detector distance was 100 mm, and a parallel x-ray beam was simulated using a cone with an extremely small cone angle (0.001 degrees or 17 microradians). In addition to the source and x-ray screen, two different ideal detectors were used to monitor the x-ray distributions: one detector was a plain of infinite lateral extent which was positioned above the x-ray source. This detector effectively measured the x-ray fluorescent re-emission emanating from the front surface of the x-ray screen. Another ideal detector of infinite lateral extent was placed under the x-ray screen, and this was used to measure the transmission of x-ray photons through the screen.

The Monte Carlo simulations performed on a 333 MHz pentium-based personal computer running NT 4.0 (Microsoft Corporation, Redmond, WA). A significant amount of custom software (Visual C/C++ 5.0, Microsoft Corporation, Redmond, WA) was used for the generation of the input script files and the analysis of the output results of the TART 97 Monte Carlo package.

## Results

The energy deposition characteristics of a  $\text{Gd}_2\text{O}_2\text{S}$  screen are shown as a function energy energy in Figure 16. The primary absorption and transmission curves as seen on this figure are predictable. The backscattered energy just above the K-edge of Gd at 51 keV is approximately 15% of the incident energy of the x-ray beam, and this backscatter is in this case almost completely due to x-ray fluorescence (technically not "scatter", but for this discussion it is included in the backscatter measurement).

The Monte Carlo code could deposit the photoelectric absorption energy locally and not track the characteristic emission, or it could track it. These two options result in the data shown in Figure 17, noting the logarithmic ordinate axis. The influence of x-ray fluorescence on the radial distribution of x-ray energy in the screen is approximately an order of magnitude greater than the contribution of Rayleigh and Compton scattering, combined.

The radial distribution of x-ray energy as a function of screen thickness is shown in Figure 18, for screens varying in thickness from  $30 \text{ mg/cm}^2$  to  $120 \text{ mg/cm}^2$ . The thicker screens experience a greater dispersion of the x-ray energy that is reabsorbed, causing a broader point spread function.

A comparison of different phosphor materials at 55 keV, as one example, is illustrated in Figure 19. Here, it is apparent that at this energy the  $\text{Gd}_2\text{O}_2\text{S}$  and  $\text{CsI}$  phosphors have broader point spread functions. The 55 keV photon is just above the k-edges of these two phosphors, but 55 keV is below the K-edges of the principal absorbing elements in  $\text{ThO}_2$ ,  $\text{YTaO}_4$ , and  $\text{CaWO}_4$ .

## Discussion

The spatial redistribution of x-ray fluorescent energy is a subtlety in terms of the performance of a screen, however the results demonstrate that at some energies up to 15% of the incident energy is lost from the screen due to fluorescence. The point spread distribution of the reabsorbed x-ray fluorescence is probably of minor consideration compared to the spread of the optical light photons (which was considered in this study). However, reabsorbed x-ray fluorescence not only degrades spatial resolution, but it induces a form of correlated noise in the image which will have a negative impact on the detective quantum efficiency performance of the imaging system. Further analysis of the noise implications of x-ray fluorescence is currently in progress.

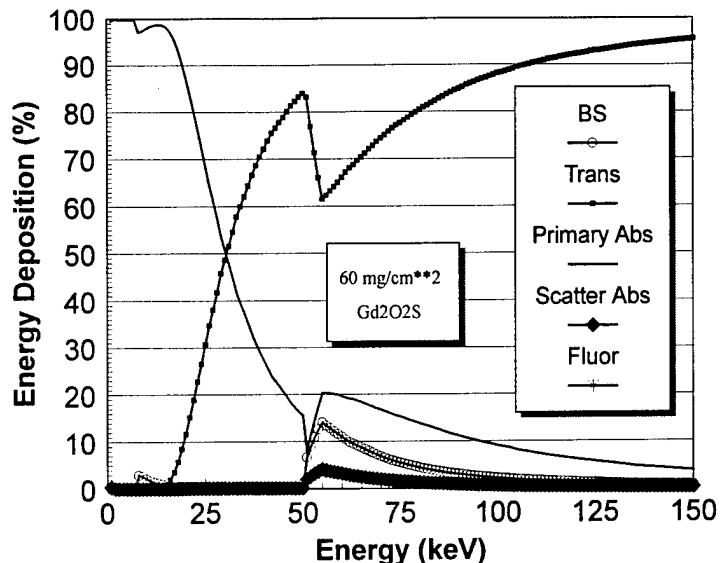


**Figure 16:** The distribution of energy deposition in a Lanex intensifying screen. The primary absorption and transmission curves of the screen are not surprising. However, just above the k-edge of Gd (50 keV), there is a large 15% fraction of essentially backscattered energy in the form of x-ray fluorescence. Approximately 5% of the fluorescent x-rays at 51 keV are reabsorbed in the intensifying screen. This reabsorption contributes both to a slight loss in spatial resolution, but more importantly the redistributed x-rays are the source of correlated noise in the image.

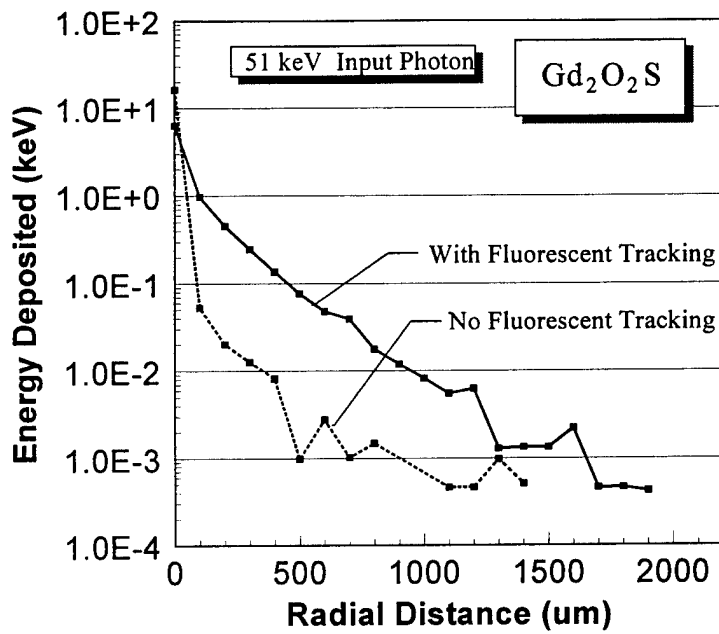


Figure 17: A plot of the radial distribution of energy for an incident beam of 51 keV (just above the K-edge of Gd). Rayleigh and Compton scatter spread is computed with the x-ray fluorescence flag turned off on the Monte Carlo simulations, and the effect of fluorescence can be included as well (“with”). The fluorescence is clearly the majority of the reabsorbed energy as shown on this semi-logarithmic graph.

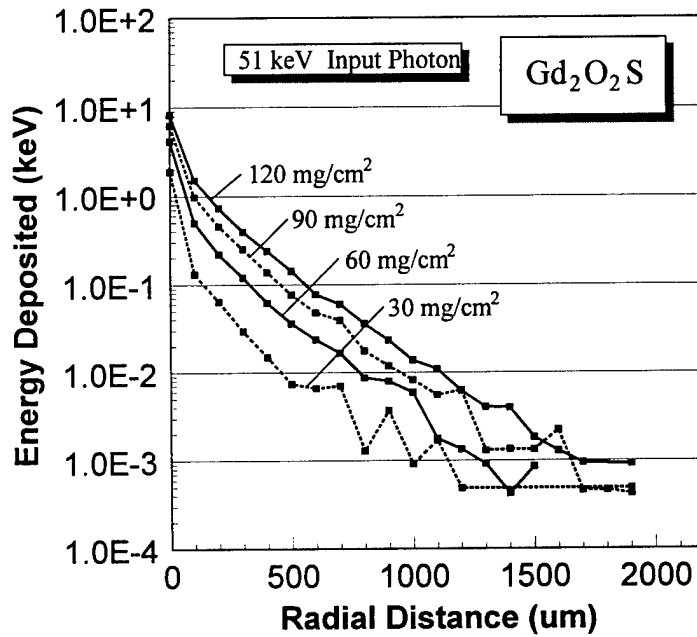
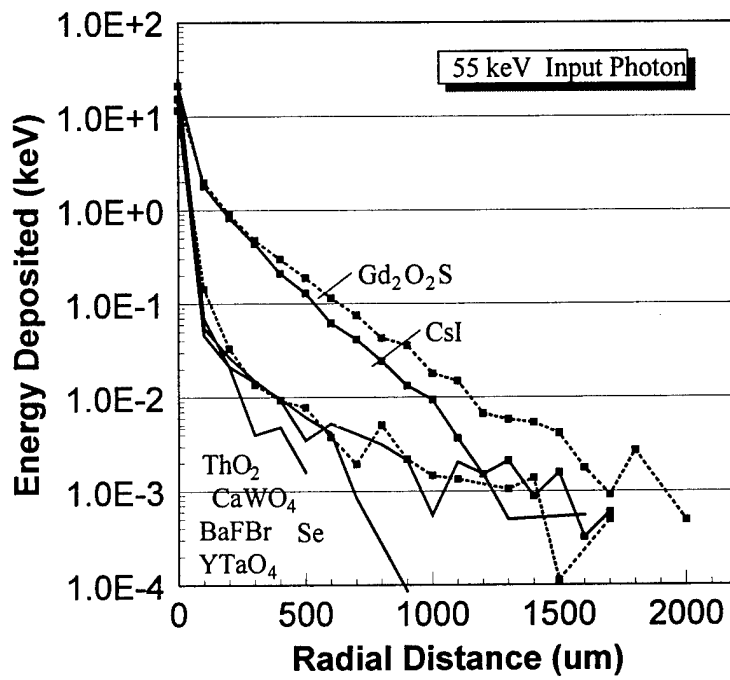


Figure 18: The radial distribution of re-absorbed energy is illustrated for Gd<sub>2</sub>O<sub>2</sub>S screens of various screen thicknesses. Thicker screens (120 mg/cm<sup>2</sup>) have approximately 10 times the re-absorbed x-ray fluorescence as thin screens (30 mg/cm<sup>2</sup>).



**Figure 19:** The radial distribution of re-absorbed energy is illustrated for a variety of 90 mg/cm<sup>2</sup> intensifying screens and direct detectors (Se). The distribution is broader for phosphors where the input x-ray energy is above the K-edge, due to the predominant contribution of the photoelectric induced fluorescent x-ray to the point spread function. The 55 keV input photon is lower than the K-edge of the heavier element phosphors (ThO<sub>2</sub>, CaWO<sub>4</sub>, and YTaO<sub>4</sub>). The low K-edges and x-ray fluorescent energies of BaFBr and Se result in less spread of the fluorescent x-rays since at low energies the attenuation coefficient of the phosphors is high.

## Breast Phantom Development

A breast phantom was developed for the evaluation of the dual energy imaging procedures. In the study section comments concerning this grant, the panel suggested that dual energy mammography was premature for a limited clinical trial. Therefore, we have concentrated on phantom studies. However, phantoms useful for the evaluation of dual energy mammography do not exist commercially. The most difficult aspect of phantom development is that the substances which are used to mimic the components of the breast, specifically the skin layer, adipose, glandular fractions, and calcifications, need to emulate the physical composition (atomic number and density) of the breast to the extent possible. It would also be desirable to produce breast compositions of different types, for example predominantly adipose or predominantly glandular.

Hammerstein et al(28) have reported on the composition and density of the various components of the breast. These values were used to compute the table given below, which gives the composition of breast tissues as a function of the glandular fraction.

---

**Table 1:**

Weight fractions of elements (H, C, N, O and P), and total tissue density,  $\rho_{\text{total}}$ , as a function of glandular weight fractions,  $f_g$ .

$f_g$ (%)	$\rho_{\text{total}}$	H	C	N	O	P ("ash")
0%	0.9301	0.112	0.619	0.017	0.251	0.001
10%	0.9399	0.111	0.576	0.019	0.294	0.001
20%	0.9501	0.110	0.532	0.020	0.336	0.002
30%	0.9605	0.109	0.488	0.022	0.379	0.002
40%	0.9711	0.108	0.445	0.023	0.421	0.003
50%	0.9819	0.107	0.401	0.025	0.464	0.003
60%	0.9930	0.106	0.358	0.026	0.507	0.003
70%	1.0044	0.105	0.315	0.028	0.549	0.004
80%	1.0160	0.104	0.271	0.029	0.592	0.004
90%	1.0278	0.103	0.227	0.030	0.634	0.005
100%	1.0400	0.102	0.184	0.032	0.677	0.005
SKIN	1.0900	0.098	0.178	0.050	0.667	0.007

There are many tissue-like substances available at the grocery store, and after a fair amount of *ad hoc* experimentation with commonly available tissue-emulating substances, we found that gelatin and lard were excellent examples of glandular tissue and adipose tissue, respectively. We also evaluated various combinations of cheese, cottage cheese, lunch meats, mayonnaise (84% fat), olive oil and tofu. While olive oil had the correct density and composition to emulate fat, its liquid and buoyancy characteristics resulted in a phantom where the glandular and adipose phases would separate over a period of time.

While a complete elemental analysis of these substances was beyond present resources, gelatin is essentially water with a small component of protein (collagen), and the attenuation properties of water are known to be very similar to glandular tissue(28). Lard on the other hand, is an extract of mammalian adipose tissue and therefore differences between lard and the adipose tissue in the breast in terms of composition are thought to be minor. The density of breast adipose tissue, from Hammerstein, is 0.93. Samples of lard were evaluated for density using standard weighing and volume displacement techniques and a density of  $0.915 \text{ g/cm}^3$  was found, only a 1.6% difference. The gelatin was also measured and found to have a density of  $1.05 \text{ g/cm}^3$ , a 0.95% difference from Hammerstein's reported value of  $1.04 \text{ g/cm}^3$ . By varying the relative quantities of the gelatin and lard, a breast of any composition could be constructed. Very importantly, the gelatin and lard mixture could be stirred up to achieve a stable, heterogeneous distribution with semi-realistic mammographic appearance. The breast studies presented in this report made use of a breast phantom carefully measured to be 50% glandular and 50% adipose.



**Figure 20:** A photograph of the dual energy breast phantom developed for this research. The phantom has an outer plexiglass layer, and is a heterogeneous mixture of lard (adipose tissue) and gelatin (glandular tissue).

The Monte Carlo studies described in a previous section made use of a mathematical phantom illustrated in Figure 1. In our initial experimentation in making a

breast phantom suitable for dual energy imaging, the tissue ingredients were molded into plastic containers (standard semispherical kitchen bowls) or injected into rubber balloons. While these techniques worked and in particular the balloon approach allowed the breast phantom to be compressed, it was difficult to achieve the well-defined shape of the semicircular compressed breast as illustrated in Figure 1. An act of shear luck then occurred, when the PI found a plastic container with nearly identical dimensions as the mathematical phantom. The overall thickness of the phantom breast was 6.0 cm, and the length along the baseline was 16.5 cm. The radius of curvature in the projection dimension of the breast phantom was 8.6 cm, very close to the 8.0 cm mathematical phantom used in the Monte Carlo simulations. The plexiglass container measured 210  $\mu\text{m}$  thick, and although this “skin” is not equivalent to the 4 mm skin thickness assumed by Wu, Barnes, and Tucker (5) and by the Monte Carlo studies reported above, this has little practical effect in this phantom study. This is because the ~3.7 mm layer of lard and gelatin which is in contact with the plexiglass housing can just be assumed to be skin, since in a phantom the dosimetry is not critical. The difference will have negligible influence in the imaging experiments.

## Detector Description and Configuration

The original concept of the detector for this proposal (as reflected by the title of the grant) was to use a single x-ray pulse and dual CCD cameras, which simultaneously image the front and back intensifying screen in a sandwiched detector configuration. Such a detector system was in fact designed and built, and this was reported in previous annual reports. Figure 21 is provided here which outlines the original proposed geometry. When the grant was written in 1993, there was a limited selection of technologies available to produce digital mammographic images, and CCD cameras were the obvious choice at that time. However, after the CCD based dual energy detector system was built and tested, a new technology of x-ray detector system based on amorphous silicon thin film transistor (a-Si TFT) arrays emerged in the literature and at national conferences. Simultaneous to these developments, it became apparent that the DQE performance of the rear detector system in the sandwiched detector design was substantially compromised by the attenuation of x-ray photons in the front detector and inter-detector filter. In addition to the poor rear-detector DQE performance, the single x-ray pulse, sandwich detector design is inherently limited in terms of the energy separation achievable. The only way to improve energy separation, by increasing the inter-detector filtration, caused a further reduction in the DQE performance in the rear detector.

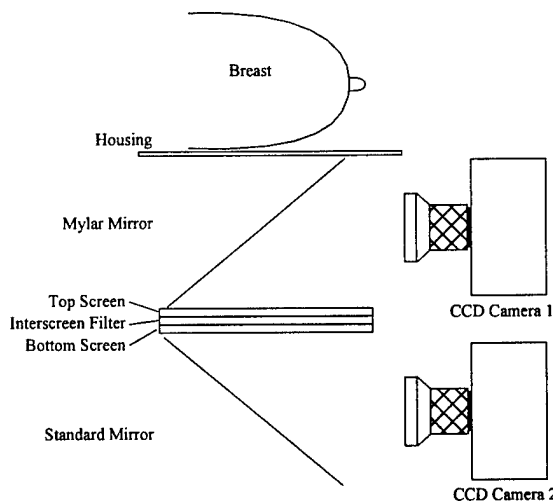


**Figure 21:** A diagram showing the geometry of the single x-ray pulse, dual sandwiched detector design that was the original goal of this grant. Not only does the rear screen DQE suffer from the heavy absorption of the x-rays in the front detector and inter-screen filter, the magnification of the breast required by the front mirror and reflection geometry poses an additional problem.

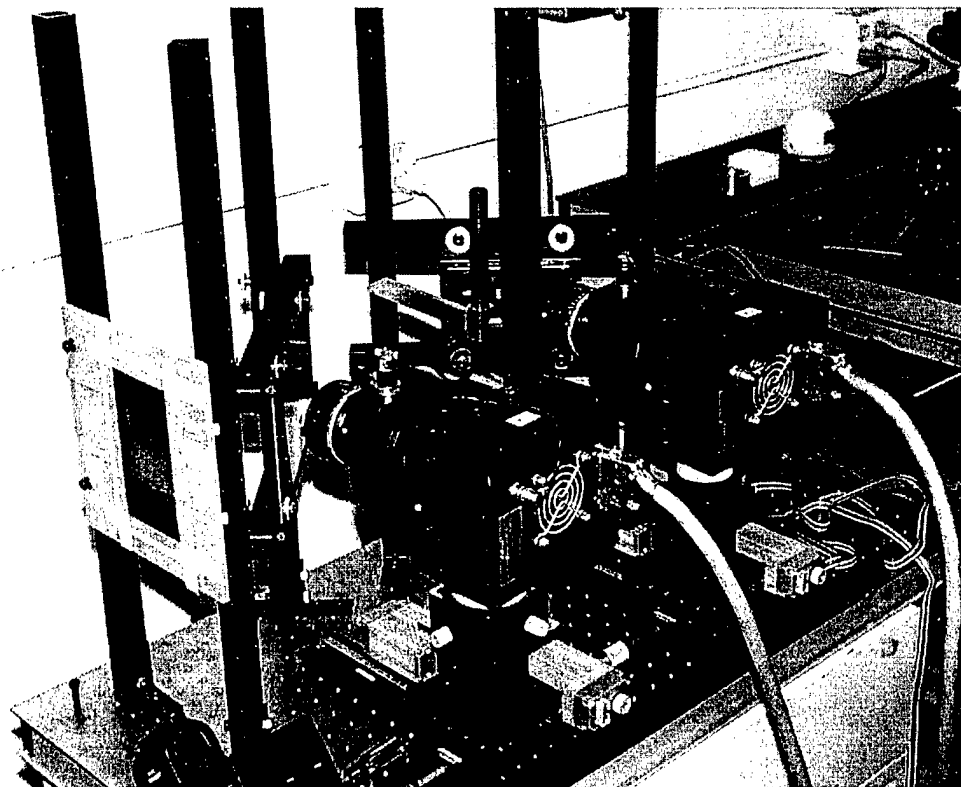


**Figure 22:** The original dual CCD detector system, designed for single-pulse dual energy acquisition.

In hind site these observations were predictable. Nevertheless, these factors led us to explore the use of an a-Si TFT technology, combined with dual x-ray pulses and switched kVs. As mentioned in the introduction, colleagues (Seibert and Alvarez) working in the PI's shared lab (with Seibert) have computer interfaced a rapid kV switching control system to the Toshiba constant potential generator in the laboratory. The 30 msec switching time achieved by Drs. Seibert and Alvarez for their research in dual energy chest radiography lends credibility to the notion that rapid kV switching(1) can be used for dual energy mammography as well.

Although a-Si TFT systems are presently only available in research laboratories or at very high costs, last year the PI was approached by Varian Imaging Products to evaluate an a-Si TFT system that they are manufacturing. The PI was awarded a small grant to evaluate the a-Si TFT system (this work is now done), but as a side benefit of that project the Varian a-Si TFT system has been and currently is available in the PI's laboratory for this project. The Varian a-Si TFT system is based on the dpiX TFT technology(32,33), and is composed of a 1536 by 1920 array of 127  $\mu\text{m}$  pixels, which results in an active area ( $\sim 18 \times 24 \text{ cm}$ ) idea for mammography. While the 127  $\mu\text{m}$  pixel pitch is probably does not have the spatial resolution required for clinical digital mammography, it is sufficient enough for the proof-of-principle research of this grant. We have evaluated a variety of input screens to the system, including CsI and  $\text{Gd}_2\text{O}_2\text{S:Tb}$ . The DQE results reported below are for a  $60 \text{ mg/cm}^2$   $\text{Gd}_2\text{O}_2\text{S:Tb}$  screen coupled to the a-Si TFT system. A photograph of the a-Si TFT detector in the PI's laboratory is shown in Figure 23:

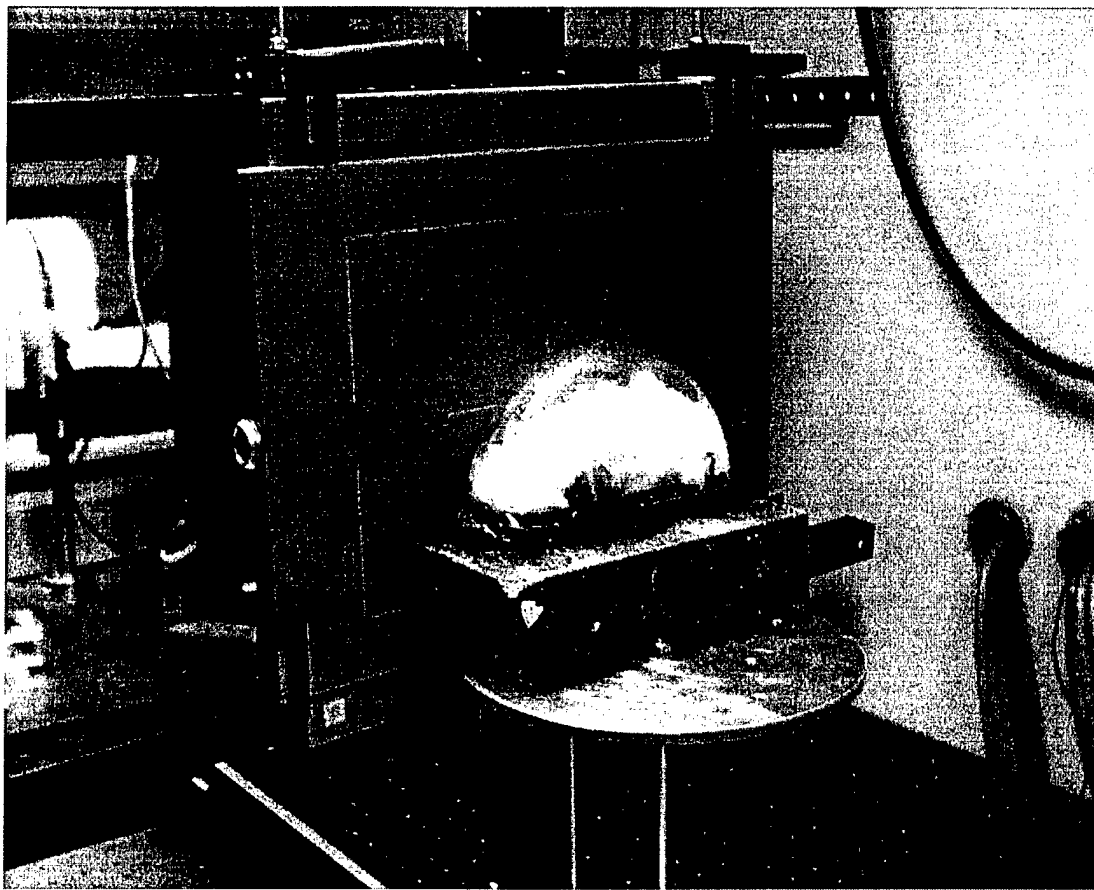


**Figure 23:** The a-Si TFT detector system is shown in the picture. The breast phantom as described above is positioned in front of the detector for the image acquisition studies described below.

## Detector Analysis

A detailed analysis of the performance of the Varian a-Si TFT system was carried out. Based on the known phosphor thickness (for the CsI input screen) and the thickness of the carbon fiber protective cover on the system, the monoenergetic and polyenergetic quantum detection efficiencies were computed as shown in Figure 24. These calculations did not include the influence of photoelectric re-emission of the characteristic photon.

The MTF was measured using the angled-slit technique, and the results at various kVs are shown in Figure 25 (left). The detective quantum efficiency was measured at various kVs as well, and these data are shown in Figure 25 (right). As would be expected, the DQE(f) is better at lower kV, reflecting better QDE (and better MTF for the 50 kV case).

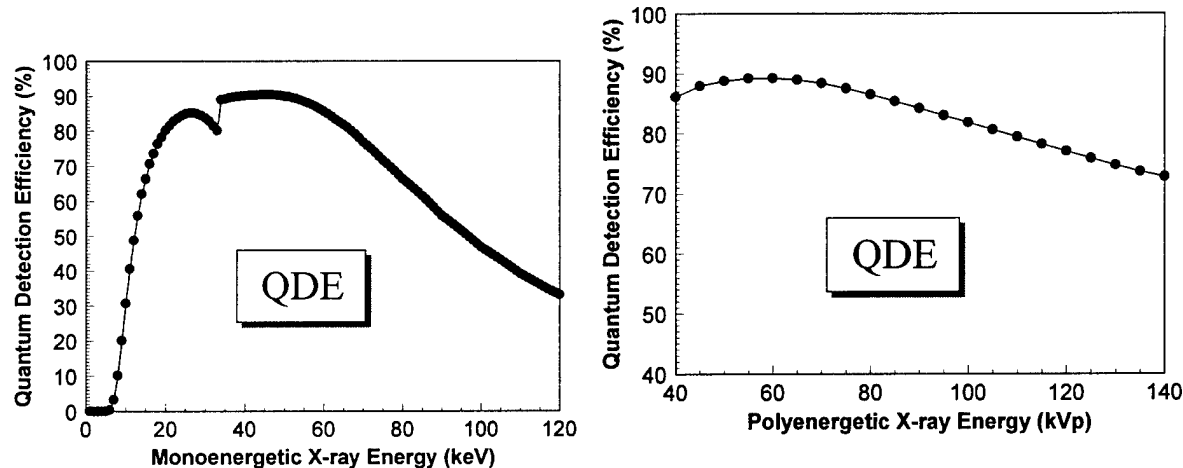


**Figure 24:** The quantum detection efficiency of the a-Si TFT system was calculated assuming a CsI input phosphor for demonstration. The monoenergetic QDE values are shown in the figure on the left, and the polyenergetic values (for tungsten target spectra) are shown on the right.

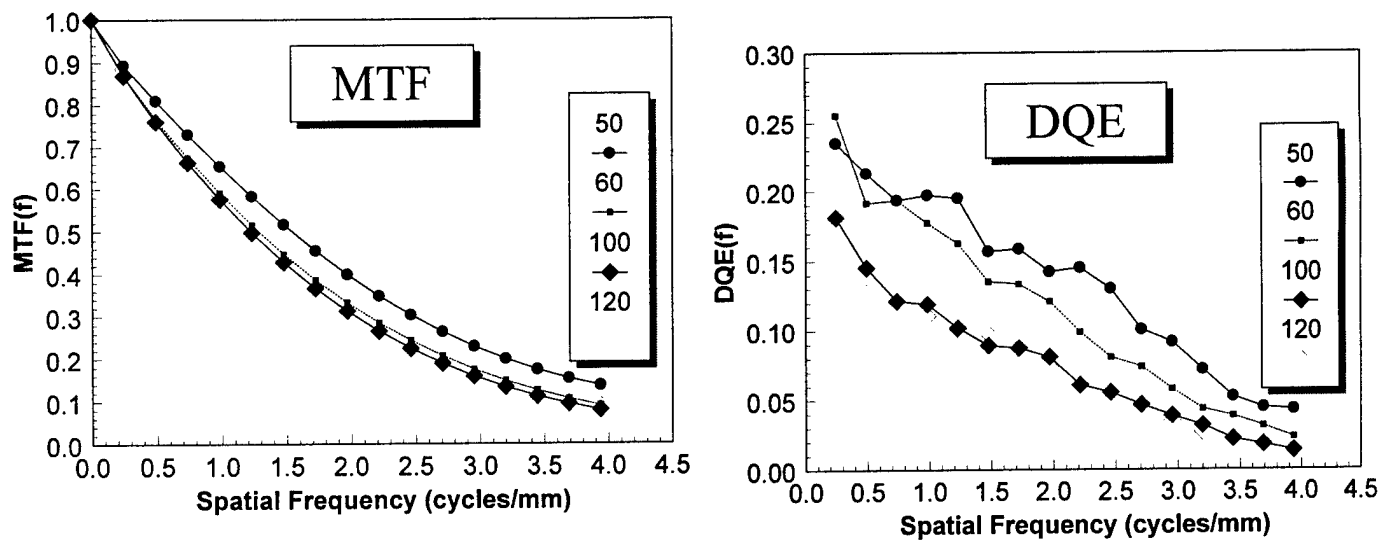


**Figure 25:** The MTF and DQE of the a-Si TFT system in the PI's laboratory. The MTF is only slightly dependent upon the beam energy, and demonstrates between 10% - 20% modulation at Nyquist (~4 lp/mm). The DQE values are shown in the figure on the right, and as expected the DQE values for lower energy beams are higher. These data were calculated on a a-Si TFT system using a  $60 \text{ mg/cm}^2 \text{ Gd}_2\text{O}_2\text{S}$  screen.

## Dual Energy Images

Images of the breast phantom were acquired using the Varian a-Si TFT detector system at a range of kVs. Whereas it would be desirable to make use of a molybdenum anode x-ray tube for the low energy image acquisition, changing x-ray tubes would make image registration difficult. Furthermore, changing x-ray tubes per se during a switched-kV study is not practical clinically where short dual-image acquisition times are necessary to prevent patient discomfort and motion.

Images were acquired over the range of kVs from 50 kV (lowest available on our constant potential generator) to 120 kV, in ~5 keV steps. For the discussion below, only the 50 kV and the 120 kV images were used. The two spectra corresponding to these two acquisitions were computed, and are shown in Figure 26. Using the 6 cm, 50% glandular tissue Monte Carlo D<sub>gN</sub> values described in the first section of this report, the estimated glandular dose for the 50 kV acquisition was 23.5 mRad. The glandular dose for the 120 kV acquisition was computed as 11.6 mRad.

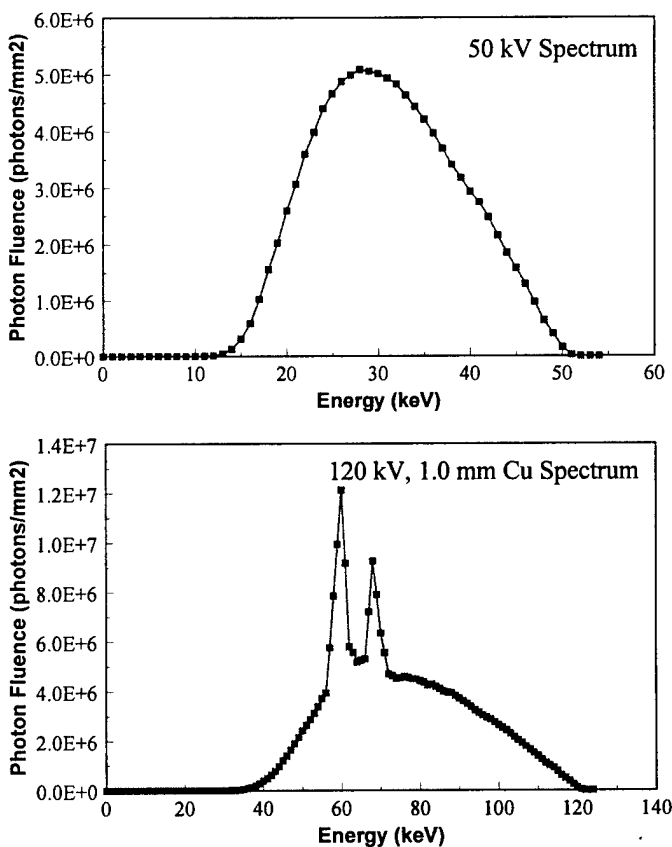


**Figure 26** The x-ray spectra corresponding to the two different x-ray pulses are shown. These spectra are estimated using a spectral model developed by the PI, using the x-ray system used for the images. The measured HVLs and kVs of the actual x-ray spectra correspond exactly to the HVLs and kVs that were computed and are shown here.

The x-ray spectra used to produce the dual energy image pairs were analyzed, and the estimated DgN values corresponding to each beam were 508.9 mRad/R for the 50 kV beam (HVL=1.47 mm Al), and 997.4 mRad/R for the 120 kV beam hardened with 1.0 mm of copper (HVL=11.17 mm Al). The entrance exposures for these beams were measured (estimated from related measurements) as 9.25 mR and 2.32 mR, respectively for the 50 and 120 kV beams. Each image was averaged 5 times at these entrance exposures, making the integrated exposures 46.25 mR for the 50 kV beam and 11.6 mR for the 120 kV beam. Therefore, by multiplying the ESE by the DgNs the estimated glandular dose to the phantom was 23.5 mRad for the 50 kV beam, and 11.65 mRad for the 120 kV beam, for a total glandular dose for the procedure of 35.15 mRad. Clearly, this is a low dose to the breast. However, it is low for two reasons: (1) Extremely low ESE values were used with the digital receptor, and: (2) Much higher kV's than those found typically in mammography. This issue will be more fully explored below.

The images were acquired, and a region of interest in the upper left corner of the images, well outside the anatomy, was integrated to compute an average background or  $I_o$  value. The raw images,  $I_{raw}$ , were then renormalized,  $I_{norm}$ , via:

$$I_{norm} = \text{LN} \left( \frac{I_o}{I_{raw}} \right)$$

The normalized images were subtracted using the simplified dual energy subtraction approach:

$$I_{sub} = I_{norm}^{50kV} - R I_{norm}^{120kV}$$

The subtracted image could then be inverted in contrast, and was renormalized to optimize the display gray scale.

The 50 kV image is illustrated in Figure 27, and the 120 kV image is illustrated in Figure 28. It is clear that the contrast in the 50 kV image is higher than that in the 120 kV, as expected.

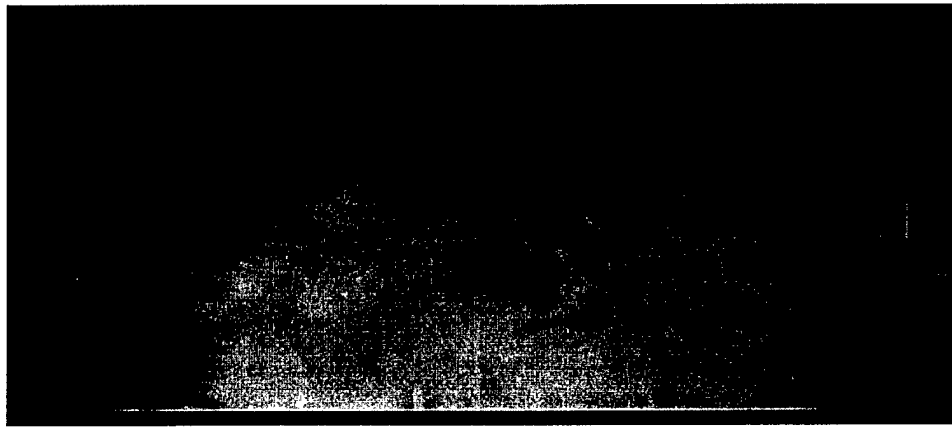


**Figure 27** An image of the 50% glandular breast phantom, acquired at 50 kV with no added filtration (HVL=1.47 mm Al) is shown. There is a calcium based step wedge on the left of the image, and a calcium ramp template on the right. An area of significant adiposity exists near the center of the breast “parenchyma”.

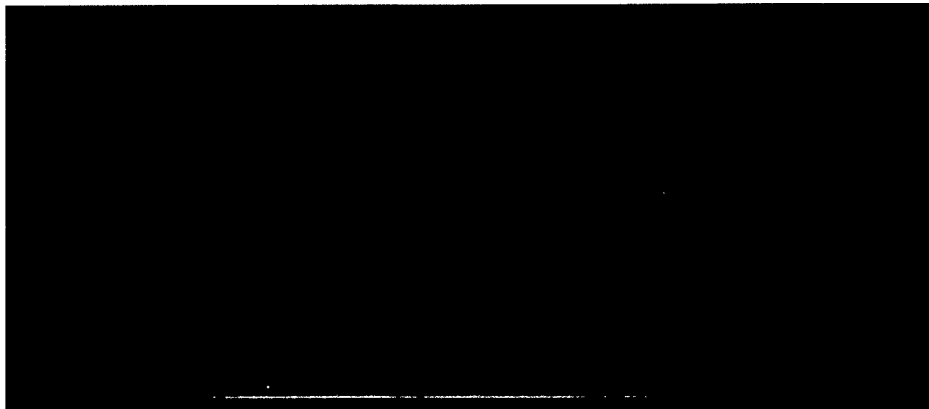


**Figure 28:** An image of the same phantom in the same position, acquired at 120 kV with added copper filtration (HVL=11.17 mm Al) is shown. This image demonstrates markedly reduced contrast compared to the 50 kV image, as one would expect.



**Figure 29:** This figure demonstrates the dual energy subtraction image of the breast phantom. The image still has “texture” over and above the presence of the calcifications that are visible. The step wedge on the left, which is calcium-based, clearly has more contrast than in either of the two raw images. Furthermore, the adipose region towards the center of the image, which was displayed quite prominently in the two raw images, is virtually eliminated in this subtraction image.

## Discussion

The optimization procedures for the dual energy acquisition have yet to be performed, however all of the mathematical and experimental tools are now in place and these studies will be conducted very shortly. Based on previously published work in this area by the PI(34), the optimal monoenergetic energies for dual energy mammography (4 cm thick breast) are 19 keV and 74 keV. The first energy, 19 keV, is achievable using a conventional mammography x-ray systems (Mo/Mo anode/filter combination), while the second energy, 74 keV, is achievable using a typical diagnostic x-ray system (W/Al anode/filter combination). The practical problem arises because two x-ray machines cannot be used, because alignment of the focal spots between the two exposures would be both impractical and difficult to achieve. The solution would appear to be to use a tungsten target, beryllium windowed x-ray tube on a system capable of switching kVs and filter material in a short period of time. However, in our laboratory we presently do not have a Be-windowed W anode tube. What is available experimentally is a conventional Mo/Mo mammography system (General Electric 500T and 600T systems are both available in the PI’s laboratory), and a Toshiba 2000 mA constant potential generator with kV settings available between 50 kV and 124 kV. The experimental images were acquired above using the Toshiba CPG, however experiments will soon be conducted using the mammography systems at for example 26 kV and 39 kV with different filtration materials.

## CONCLUSIONS

### Scientific Outlook

Dual energy mammography remains an exciting and feasible modality, and may be a practical adjunct or replacement for women who have exceptionally dense or thick breasts. Our research has focussed on both the computer simulation of dose and technique optimization, and on the development of a physical detector system in the laboratory. In the early years of the grant, we concentrated on a CCD based, single x-ray pulse, dual-sandwiched detector system for dual energy acquisition. In building and testing this system, we realized that an alternate design would be better in terms of dose efficacy (based on DQE analysis), and as explained previously, the a-Si TFT technology became available to us in the laboratory for this project. With the detector system functioning in our laboratory, we now turn our attention completely to optimizing the dual energy techniques in terms of beam energies.

In last year's annual report, we reported that we were unable to produce published results on the computer simulation for radiation doses to the breast. This situation has been corrected and we now are within 5% or better of the results of Wu, Barnes and Tucker(5) and those of Dance(6). After confirming our Monte Carlo approach, we extended the dose data to both higher energies and thicker breasts. We are prepared to use our calculated DgN values, the spectral models (25, 26) and attenuation coefficients(27) developed previously under this grant funding to finalize the technique optimization of both single and dual energy digital mammography acquisition.

The development of better dual energy subtraction and display methods will also be addressed aggressively in this last year of the grant.

### Progress and Future Directions

The table given below summarizes our progress as we enter the fifth, no-cost extention year of the grant period. The design, construction, and analysis of the CCD based detector system was completed in previous years, and based on those results we have now shifted to the a-SI TFT detector system. The TFT system's design, construction and analysis have been completed. Varian designed and built the system, but the PI continues to work with the Varian R & D scientists in the evaluation of the system and in the design of the phosphor. (CsI and  $Gd_2O_2S$  phosphors tested to date). Thus, Tasks 2 and 3 are completely finished. In addition, the study section who originally evaluated the proposal suggested that Task 5 be eliminated, and in fact the money was cut reflected that suggestion. The PI, working with Army staff, formally requested the elimination of Task 5 from the Statement of Work, and this was approved by the Army last year.

Thus, Task 1 remains to perform in its entirety. Fortunately, the calculation of accurate DgN values at higher x-ray energies has been performed (the hard part), and now

this data is ready to be exploited in Tasks 1.1 and 1.2. Preliminary results, for example, were presented above concerning Task 1.2. By changing the design paradigm from single x-ray pulse/dual sandwiched detectors to dual pulsed/single detector, the analysis of the phosphor thicknesses and composition (Task 1.3) is shifted to a straightforward analysis of detection efficiency. Towards this end, the PI is currently investigating the role that x-ray fluorescence has in terms of spatial resolution and signal to noise ratio, and those results were presented above as well.

What remains to be done is Task 4 (4.1 and 4.2), and although we do have dual energy subtraction algorithms in place and working, further study will address whether or not improvements to existing algorithms can be made and whether or not they are practical.

**Table 2:**

This table describes our progress towards meeting the Statement of Work as listed in the original proposal.

Task 1	Description	Status
1.1	Most Efficient Spectrum – Dual Energy	Tools in Place, Ready to Perform
1.2	Most Efficient Spectrum – Single Energy	Preliminary data presented here, task near completion
1.3	Best Phosphor Thickness & Type	Change in acquisition paradigm eliminates this, but we're currently studying the influence of x-ray fluorescent reabsorption in screens.
1.4	Most Efficient Anti-Scatter Grid	Need to validate PI's Monte Carlo code against TART, and compute scatter tables
<b>Task 2</b>		
2.1	Design System	Done
2.2	Build System	Done
<b>Task 3</b>		
3.1	Measure MTF	Done
3.2	Measure DQE	Done
3.3	Digitize Films	Will Compare DQE's against literature instead of remeasuring DQE's for film.
<b>Task 4</b>		
4.1	Neural Networks for Dual-Energy Subtraction	Preliminary data indicated that the neural network approach is not as robust as a straightforward analytic procedure
4.2	Segment microcalcifications and study display	To be done in no cost extension year.
<b>(Task 5)</b>	Limited Clinical Trial	Task formally eliminated from SOW by US Army due to cut in funding and study section recommendation.

## REFERENCES

1. R. E. Alvarez, *Med. Phys.* **23**, 1739 (1996).
2. R. N. Kulkarni, S. J. Supe, *Phys. Med. Biol.* **29**, 1257 (1984).
3. K. Doi, H. P. Chan, *Radiology* **135**, 199 (1980).
4. D. R. Dance, *Phys. Med. Biol.* **25**, 25 (1980).
5. X. Wu, G. T. Barnes, D. M. Tucker, *Radiology* **179**, 143 (1991).
6. D. R. Dance, *Phys. Med. Biol.* **35**, 1211 (1990).
7. E. L. Gingold, X. Wu, G. T. Barnes, *Radiology* **195**, 639 (1995).
8. X. Wu, E. L. Gingold, G. T. Barnes, D. M. Tucker, *Radiology* **193**, 83 (1994).
9. D. R. Dance, J. Perslidén, G. A. Carlsson, *Phys. Med. Biol.* **37**, 235 (1992).
10. K. H. Ng, R. J. Aus, L. A. DeWerd, J. R. Vetter, *Radiology* **205**, 395 (1997).
11. F. Arfelli, V. Bonvicini, A. Bravin, G. Cantatore, E. Castelli, et al, *Phys. Med. Biol.* **42**, 1565 (1997).
12. A. C. Thilander-Klang, P. H. Ackerholm, I. C. Berlin, N. G. Bjurstam, S. L. Mattsson, et al, *Radiology* **203**, 348 (1997).
13. A. Calicchia, M. Gambaccini, P. L. Indovina, F. Mazzei, L. Puglianì, *Phys. Med. Biol.* **41**, 1717 (1996).
14. D. L. Thiele, A. R. Craig, *Australas. Phys. Eng. Sci. Med.* **19**, 94 (1996).
15. J. R. Gentry, L. A. DeWerd, *Med. Phys.* **23**, 899 (1996).
16. D. L. Monticciolo, P. Sprawls, B. D. Kruse, J. E. Peterson, *South. Med. J.* **89**, 391 (1996).
17. K. H. Lee, S. Kandaiya, *Appl. Radiat. Isot.* **47**, 361 (1996).
18. K. Faulkner, J. Law, K. J. Robson, *Br. J. Radiol.* **68**, 877 (1995).
19. M. A. Helvie, H. P. Chan, D. D. Adler, P. G. Boyd, *AJR. Am. J. Roentgenol.* **163**, 1371 (1994).
20. J. M. Boone, G. S. Shaber, M. Tecotzky, *Med. Phys.* **17**, 665 (1990).
21. J. M. Boone, J. A. Seibert, *Med. Phys.* **15**, 713 (1988).
22. J. M. Boone, J. A. Seibert, *Invest. Radiol.* **23**, 627 (1988).
23. D. E. Cullen, *UCRL-ID-126455, Rev 1 LLNL Document*, (1997).
24. The Monte Carlo code TART97 was purchased on CD ROM from Oak Ridge National Laboratory. The contact there is: <http://www-rsicc.ornl.gov/rsic.html>.
25. J. M. Boone, T. R. Fewell, R. J. Jennings, *Med. Phys.* **24**, 1863 (1997).
26. J. M. Boone, J. A. Seibert, *Med. Phys.* **24**, 1661 (1997).
27. J. M. Boone, A. E. Chavez, *Med. Phys.* **23**, 1997 (1996).
28. G. R. Hammerstein, D. W. Miller, D. R. White, M. E. Masterson, H. Q. Woodard, et al, *Radiology* **130**, 485 (1979).
29. D. M. Tucker, G. T. Barnes, X. Z. Wu, *Med. Phys.* **18**, 402 (1991).
30. R. E. Johnston, D. Washburn, E. Pisano, C. Burns, W. C. Thomlinson, et al, *Radiology* **200**, 659 (1996).
31. J. M. Boone, J. A. Seibert, *Med. Phys.* **21**, 1853 (1994).
32. L. E. Antonuk, Y. el-Mohri, J. H. Siewerdsen, J. Yorkston, W. Huang, et al, *Med. Phys.* **24**, 51 (1997).

33. J. H. Siewerdsen, L. E. Antonuk, Y. el-Mohri, J. Yorkston, W. Huang, et al, *Med. Phys.* **24**, 71 (1997).
34. JM Boone, *Investigative Radiology* **26**:521, (1991)